Department of Physics and Astronomy
Heidelberg University

Bachelor Thesis in Physics
submitted by

Tim Ehret

born in Freiburg im Breisgau (Germany)

2022

Optimizing elementary quantum gates

This Bachelor Thesis has been carried out by Tim Ehret at the
Institute for Theoretical Physics in Heidelberg
under the supervision of
Prof. Sandro Wimberger
Prof. Luca Amendola

Zusammenfassung

Der zentrale Gegenstand dieser Arbeit ist die Optimierung und Beschleunigung eines Quantengatters. Neutrale Rydberg-Atome bilden die Grundlage für unsere Simulationen; ein Qubit kann in der Hyperfeinstruktur eines Rydberg-Atoms encodiert werden. Für die Implementierung eines CZ-Quantengatters kann ein starker Rydberg-Blockademechanismus ausgenutzt werden; wir diskutieren unter anderem Phasenfehler, die durch eine unzureichend starke Blockade entstehen können. Darüber hinaus beschleunigen wir ein CZ-Quantengatter mit „counterdiabatic driving“ und prüfen, ob die Stabilität durch die Beschleuningung beeinträchtigt wird. Dieses CZ-Phasengatter erweitern wir anschließend zu einem CNOT-Gatter.

Abstract

The focus of this thesis lies on the optimization and acceleration of a quantum gate. Our simulations are based on neutral Rydberg atoms; a qubit can be encoded in the hyperfine structure of a Rydberg atom. To implement a CZ quantum gate, one can exploit a strong Rydberg blockade mechanism. We discuss phase errors that can arise if the blockade is not sufficiently strong. Furthermore, we accelerate a CZ quantum gate by means of counterdiabatic driving and check that the acceleration of the gate does not compromise its stability. Additionally, we extend the accelerated CZ phase gate to obtain a CNOT gate.

Contents

1. Introduction

The impact of a functioning large-scale quantum computer can hardly be overestimated. The most prominent application is the prime factorization of large numbers via Shor's algorithm [1] - a task whose unfeasibility in classical computing is the basis for current cryptosystems. Further applications include the simulation of proteins [2], optimization problems [3], search problems [4] etc. Large-scale quantum computers that can cope with the aforementioned tasks are not yet within reach, but there has been steady progress toward noisy, intermediate-scale quantum computers (NISQ) that will feature 50 to a few hundred qubits [5]. A great variety of physical platforms for quantum computing have been proposed and studied; among them are trapped ions [6], superconducting circuits [7], quantum dots [8] and neutral atoms [9]. Although some of these platforms seem to be more promising than others, none of them has prevailed so far. In this thesis, we will focus on neutral Rydberg atoms. The first proposals to use these atoms for quantum computing were put forward more than twenty years ago, but a lot of progress has been made recently.

In general, a quantum algorithm can be expressed as a series of measurements and single / two-qubit quantum gates [10, pp. 171-172]. On the Rydberg platform, these quantum gates can be implemented via laser fields that couple certain energy levels of the atoms. Quantum gates that are able to create entangled states are of particular interest; to implement these gates, we take advantage of the Rydberg blockade mechanism, which will be discussed later on. As we will see, this blockade mechanism is not perfect, which gives rise to phase issues. Two sections of this thesis are dedicated to the discussion of this imperfection.

Qubits can be manipulated via different types of laser pulses. We are interested in adiabatic rapid passage (ARP) pulses. As the name suggests, these pulses rely on an adiabatic process, hence there is an adiabaticity condition that must not be violated. This condition limits the speed of the pulse operation. It is clear that we want to keep the total gate operation time as low as possible to avoid decoherence, thus we are looking for ways to accelerate ARP-based quantum gates. A method that is known as counterdiabatic driving [11] allows us to arbitrarily accelerate adiabatic evolution; we want to apply this method to an adiabatic two-qubit CZ phase gate. This particular phase gate is of interest to us because it provides the foundation for one of the most important two-qubit gates: the CNOT gate. The implementation of the CNOT gate is covered in the fourth chapter. Once we have built a CNOT gate, we have the means to simulate a small three-qubit quantum error correction (QEC) circuit that can correct bit flip errors on a single qubit. While QEC schemes offer great protection against all kinds of errors that can occur due to noise or faulty gate operation, they require substantial resources in terms

of additional ancilla qubits. Given the relatively low count of qubits in the latest quantum computers, it is clear that qubits cannot be allocated for error correction purposes yet, but QEC schemes will be an integral part of quantum computers beyond the NISQ era.

To avoid confusion, we make a brief remark about the terminology: we will refer to the CZ phase gate that is implemented by adiabatic rapid passage pulses as "adiabatic" CZ gate. This is not to be confused with adiabatic quantum computing [12]. The latter is a different approach to quantum computing that does not rely on quantum gates, but instead on quantum annealing.

The thesis is structured as follows: after covering some basics in the second chapter, we will discuss the optimization and acceleration of the (non)adiabatic CZ gate in the third chapter. Afterwards, we will extend the accelerated CZ gate in chapter four to obtain a CNOT gate; in addition to that, chapter four contains a section about quantum error correction.

2. Preliminaries

The objective of this chapter is threefold: we want to discuss some basics of quantum computing, introduce the Rydberg platform featuring cold neutral atoms, and review the concept of counterdiabatic driving. After presenting a brief selection of the various physical platforms for quantum computing, we focus on the Rydberg platform and derive the Hamiltonian that we will use in the following chapters. Subsequently, we describe how we can manipulate qubits using π pulses and adiabatic rapid passage (ARP) pulses. This is followed by a section about counteradiabatic driving, which provides us with a useful tool to build fast adiabatic gates. The chapter ends with a section about quantum gates, in which we will particularly explain the composition of the CNOT gate. This composition determines the structure of this thesis; we will gradually build a CNOT gate and use it to build a more complex quantum circuit.

2.1. Platforms for quantum computing

The realization of quantum computers is challenging; the main requirements have been characterized by DiVincenzo [13, pp. 773-779]. We need

- "A scalable physical system with well characterized qubits"
- "The ability to initialize the state of the qubits to a simple fiducial state, such as $|000....\rangle$"
- "Long relevant decoherence times, much longer than the gate operation time"
- "A 'universal' set of quantum gates"
- "A qubit-specific measurement capability"

There are various platforms that fulfill these requirements to a varying degree. The number of platform proposals is too high to give an overview in this section; we selected only a few platforms to illustrate the diversity and to highlight some of the challenges. A more detailed overview can be found in Nielsen and Chuang [10, pp. 283-352].

NMR
Nuclear magnetic resonance quantum computing is one of the most well-studied platforms. The two qubit states $|0\rangle$ and $|1\rangle$ are mapped to the Zeeman levels of nuclei in a magnetic field [14, p. 2]. In contrast to other platforms, a single

qubit is represented by a large ensemble of spins which belong to molecules in a liquid sample. Single-qubit gates can be realized via standard NMR pulses and the spin-spin coupling allows for the implementation of two-qubit gates. Due to scaling issues, NMR quantum computing is not a viable option for building large quantum computers, but NMR research gave rise to some useful tools such as composite pulses that can be adopted for other platforms [15, p. 116].

Trapped ions
The proposal to map the two states of a qubit to the internal states of cold trapped ions was put forward by Cirac and Zoller [6]. Single-qubit operations can be performed by coupling different states with lasers; two-qubit gates can be realized via the excitation of shared vibrational states. High-fidelity single-qubit gates [16],[17] and two-qubit gates [18] have already been accomplished, making trapped ions one of the most promising platforms. Even though this platform features many advantages, such as long coherence times, high-fidelity gates and high-fidelity readout, the gate operation is slow compared to other platforms and the scaling proves to be difficult once again [19, pp. 3-4].

Superconducting circuits
This type of platform is essentially based on superconducting LC-circuits that form quantum harmonic oscillators. The energy levels of a quantum harmonic oscillator are evenly spaced, which is a problem if one wants to drive only certain transitions, therefore another nonlinear element (Josephson junction) is added to the circuit to get unevenly spaced energies [20, pp. 371-373]. Coherence requires the lack of dissipation in the circuit, which is achieved by zero resistance. High-fidelity gates have been demonstrated [21], but the platform is challenged by short coherence times and noise.

Rydberg atoms
In terms of scalability, neutral atoms have more potential since they can be arranged in complex structures (as opposed to ions). Rydberg atoms can be excited to a Rydberg state $|r\rangle$ with a large principal quantum number n. The radius scales as n^2, hence the state $|r\rangle$ features a large electric dipole moment. Jaksch et al. put forward the idea to use this long-range dipolar interaction to block the excitation of surrounding atoms to the Rydberg state; this Rydberg blockade provides a way to implement two-qubit gates [9]. There are multiple ways to encode a logical qubit in the level structure of a Rydberg atom; for instance, one could encode $|0\rangle$ and $|1\rangle$ in the hyperfine structure and use a Rydberg level as an auxiliary state for two-qubit gates. Heavy alkali atoms such as Rb and Cs have favorable properties with regard to laser cooling and hyperfine structure [22, p. 2317], hence these atoms are typically used in experiments. A comprehensive review of quantum computing with Rydberg atoms was published by Morgado and Whitlock [23].

2.2. Rydberg platform

The following derivation is based on [24, pp. 13-15]. We consider a single Rydberg atom with three states $|0\rangle, |1\rangle$ and $|r\rangle$. The atom interacts with two lasers with frequencies ω_{L1}, ω_{L2} that drive the transition $|0\rangle \leftrightarrow |1\rangle$ and $|1\rangle \leftrightarrow |r\rangle$, respectively. Neglecting decay processes, the Hamiltonian of the system is given by

$$\hat{H}(t) = \sum_{n\in\{0,1,r\}} E_n |n\rangle \langle n| + \hat{d}\cdot\hat{E} \, . \tag{2.1}$$

For convenience, we set the energy of the ground state to zero. The electric field can be written as $\mathbf{E} = \mathbf{E}_{L1}\cos(\omega_{L1}t) + \mathbf{E}_{L2}\cos(\omega_{L2}t)$. By defining the Rabi frequencies as

$$\Omega_{01} = \frac{\langle 0|\, \hat{d}\hat{E}_{L1}\, |1\rangle}{\hbar} \, , \qquad\qquad \Omega_{1r} = \frac{\langle 1|\, \hat{d}\hat{E}_{L2}\, |r\rangle}{\hbar} \, , \tag{2.2}$$

we can write the Hamiltonian in matrix representation as

$$H(t) = \hbar \begin{bmatrix} 0 & \Omega_{01}\cos(\omega_{L1}t) & 0 \\ \Omega_{01}^{\dagger}\cos(\omega_{L1}t) & \omega_{01} & \Omega_{1r}\cos(\omega_{L2}t) \\ 0 & \Omega_{1r}^{\dagger}\cos(\omega_{L2}t) & \omega_{01}+\omega_{1r} \end{bmatrix} , \tag{2.3}$$

where $\omega_{01} = E_1/\hbar$ and $\omega_{1r} = (E_r - E_1)/\hbar$. We enter a reference frame that rotates at the laser frequency by applying the following unitary transformation

$$U(t) = \begin{bmatrix} 1 & 0 & 0 \\ 0 & e^{i\omega_{L1}t} & 0 \\ 0 & 0 & e^{i(\omega_{L1}+\omega_{L2})t} \end{bmatrix} . \tag{2.4}$$

The Hamiltonian transforms as $H_{\text{new}} = UH_{\text{old}}U^{\dagger} + i\hbar\dot{U}U^{\dagger}$.

$$H(t) = \hbar \begin{bmatrix} 0 & \Omega_{01}\cos(\omega_{L1}t)e^{-i\omega_{L1}t} & 0 \\ \Omega_{01}^{\dagger}\cos(\omega_{L1}t)e^{i\omega_{L1}t} & \omega_{01}-\omega_{L1} & \Omega_{1r}\cos(\omega_{L2}t)e^{-i\omega_{L2}t} \\ 0 & \Omega_{1r}^{\dagger}\cos(\omega_{L2}t)e^{i\omega_{L2}t} & \omega_{01}+\omega_{1r}-\omega_{L1}-\omega_{L2} \end{bmatrix} \tag{2.5}$$

$$= \hbar \begin{bmatrix} 0 & \Omega_{01}/2\,(1+e^{-2i\omega_{L1}t}) & 0 \\ \Omega_{01}^{\dagger}/2\,(1+e^{2i\omega_{L1}t}) & \omega_{01}-\omega_{L1} & \Omega_{1r}/2\,(1+e^{-2i\omega_{L2}t}) \\ 0 & \Omega_{1r}^{\dagger}/2\,(1+e^{2i\omega_{L2}t}) & \omega_{01}+\omega_{1r}-\omega_{L1}-\omega_{L2} \end{bmatrix} \tag{2.6}$$

The purpose of this transformation is not immediately obvious since the off-diagonal entries are still time-dependent, but now we can remove the time dependence by employing the rotating wave approximation (RWA), which states that the fast oscillating terms $e^{\pm 2i\omega_{Li}t}$ can be neglected provided that $|\omega_{01}-\omega_{L1}| \ll |\omega_{01}+\omega_{L1}|$ and $|\omega_{1r}-\omega_{L2}| \ll |\omega_{1r}+\omega_{L2}|$. Furthermore, we define the detuning as follows:

$$\delta = \omega_{01} - \omega_{L1} \, , \qquad\qquad \Delta = \omega_{01} + \omega_{1r} - \omega_{L1} - \omega_{L2} \, . \tag{2.7}$$

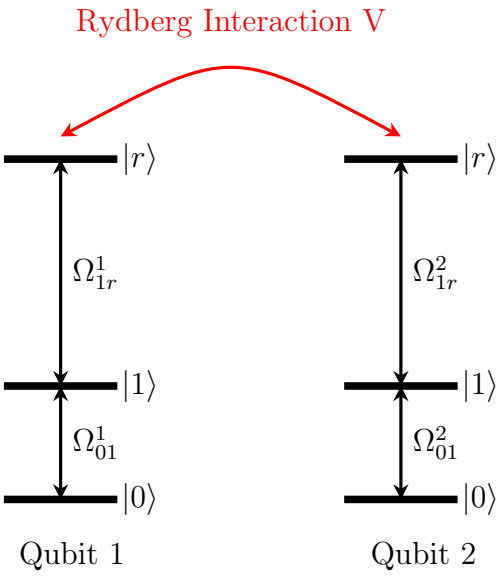

Figure 2.1.: Levels of two Rydberg atoms. The transitions are labeled with the corresponding Rabi frequency

With these changes, our final Hamiltonian reads

$$H(t) = \hbar \begin{bmatrix} 0 & \Omega_{01}/2 & 0 \\ \Omega_{01}^\dagger/2 & \delta & \Omega_{1r}/2 \\ 0 & \Omega_{1r}^\dagger/2 & \Delta \end{bmatrix} . \tag{2.8}$$

Having derived the Hamiltonian of a single Rydberg atom, we can now give the full Hamiltonian of a two-qubit system, which consists of two Hamiltonians describing the dynamics of a single Rydberg atom and an additional term that accounts for the Rydberg interaction V between the Rydberg states:

$$\hat{H} = \hat{H}_1 \otimes \mathbb{1} + \mathbb{1} \otimes \hat{H}_2 + \mathrm{V} \left|r\right\rangle \left\langle r\right| \otimes \left|r\right\rangle \left\langle r\right| \ . \tag{2.9}$$

We usually set $\hbar$ to 1, so we will express the Rydberg interaction V in GHz or MHz, as is common practice.

2.3. π pulses and ARP pulses

The standard way to induce a population transfer between two levels is to use resonant π pulses. By using the rotating frame transformation and the rotating wave approximation from the previous section, the Hamiltonian of a two-level system interacting with a laser field can be written as

$$H(t) = \begin{bmatrix} 0 & \Omega(t)/2 \\ \Omega(t)/2 & \Delta(t) \end{bmatrix} , \tag{2.10}$$

where $\Omega(t)$ is the real Rabi frequency and $\Delta(t)$ is the detuning. A complete population transfer can be achieved by applying a pulse with area $\int \Omega(t)dt = \pi$ and $\Delta \equiv 0$, hence the name π pulse. We used gaussian or discrete pulse profiles in our simulations. Another way of realizing the transfer is to use adiabatic rapid passage pulses. These pulses sweep through the resonance frequency [25, p. 147]. An example is given in Fig. 2.2; here, the Rabi frequency has a gaussian profile and the detuning is linear. Calculating the instantaneous eigenstates of the system yields

$$|\phi_+\rangle = \frac{1}{\sqrt{1+\beta_+^2}} \left(\beta_+ |0\rangle + |1\rangle\right) , \qquad |\phi_-\rangle = \frac{1}{\sqrt{1+\beta_-^2}} \left(\beta_- |0\rangle + |1\rangle\right) , \tag{2.11}$$

where $\beta_\pm = (-\Delta(t) \pm \bar{\Omega}(t))/\Omega(t)$ with $\bar{\Omega}(t) = \sqrt{\Delta(t)^2 + \Omega(t)^2}$. For small times, we have $|\Delta| \gg |\Omega|$ and $\Delta < 0$, therefore $|\phi_-\rangle \approx |1\rangle$ and $|\phi_+\rangle \approx |0\rangle$, whereas for large times, we have $|\Delta| \gg |\Omega|$ and $\Delta > 0$, leading to $|\phi_-\rangle \approx |0\rangle$ and $|\phi_+\rangle \approx |1\rangle$. The adiabatic theorem states that a system remains in its instantaneous eigenstate, provided that the change of the Hamiltonian is sufficiently slow and the spectrum consists solely of discrete, nondegenerate eigenvalues [26]. Consequently, we can transfer the population between $|0\rangle$ and $|1\rangle$ by applying the pulse adiabatically such that the system remains in its instantaneous eigenstate $|\phi_+\rangle$ or $|\phi_-\rangle$. The advantage of ARP pulses is that the fidelity of the transfer depends only weakly on the pulse amplitude, which means that ARP pulses are more robust than π pulses. This robustness does not imply that ARP pulses are superior to π pulses, since they are quite slow. Fig. 2.3 shows the result of violating the adiabaticity condition. Furthermore, π pulses are more versatile: in a two level system, we can implement any rotation around the x-axis (of the bloch sphere) with an appropriately normalized π pulse, whereas ARP pulses are only able to transfer population if the initial state is $|0\rangle$ or $|1\rangle$.

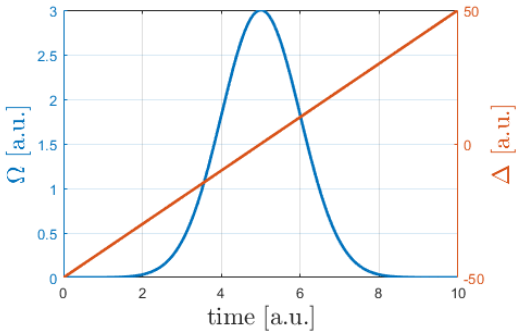

Figure 2.2.: Gaussian-shaped Rabi frequency Ω and linear detuning Δ of an ARP pulse

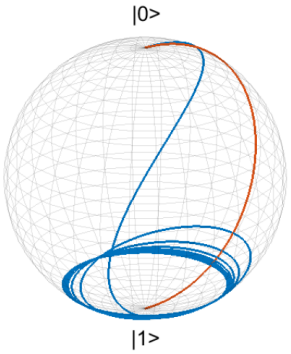

Figure 2.3.: Population transfer in a two-level system, visualized on a Bloch sphere. The red line is the result of perfect adiabatic transfer, the blue line shows imperfect transfer due to a violation of the adiabaticity condition

2.4. Counterdiabatic driving

Among others [27], Michael Berry proposed a powerful method to avoid unwanted transitions between instantaneous eigenstates entirely, enabling us to complete adiabatic evolutions arbitrarily fast [11]. This method is known as "counterdiabatic driving", "transitionless quantum driving" or "superadiabatic driving". We follow Berry's short derivation: consider an arbitrary Hamiltonian $\hat{H}_0$ with nondegenerate, discrete eigenvalues and instantaneous eigenstates $|n(t)\rangle$,

$$\hat{H}_0(t) = E_n(t)\,|n(t)\rangle \ . \tag{2.12}$$

In the adiabatic limit, the system remains in eigenstate $|n(t)\rangle$ if it is initially prepared in $|n(0)\rangle$, gaining the following phase $\gamma_n(t)$ in the process:

$$|\psi_n(t)\rangle = e^{i\gamma_n(t)}\,|n(t)\rangle \ , \quad \text{where} \quad \gamma_n(t) = -\frac{1}{\hbar}\int_0^t E_n(t')dt' + \int_0^t \langle n(t')|\partial_{t'} n(t')\rangle\, dt' \ . \tag{2.13}$$

The first term accounts for the dynamical phase, the second term accounts for the geometric phase. Berry constructs a new Hamiltonian $\hat{H}(t)$ such that the states $|\psi_n(t)\rangle$ are not just the result of an adiabatic evolution; the states $|\psi_n(t)\rangle$ become the exact solution of the Schrödinger equation. To find $\hat{H}(t)$, Berry defines the unitary operator

$$\hat{U}(t) = \sum_n e^{i\gamma_n(t)}\,|n(t)\rangle\,\langle n(0)| \tag{2.14}$$

and notes that any unitary operator satisfies

$$i\hbar\partial_t\hat{U}(t) = \hat{H}(t)\hat{U}(t) \ , \quad \text{where} \quad \hat{H}(t) = i\hbar(\partial_t\hat{U}(t))\hat{U}^\dagger(t) \ . \tag{2.15}$$

Therefore, $\hat{H}(t)$ can be obtained by substituting Eq. (2.14) in Eq. (2.15), which yields:

$$\hat{H}(t) = \underbrace{\sum_n |n(t)\rangle\, E_n(t)\,\langle n(t)|}_{=\hat{H}_0} + \underbrace{i\hbar\sum_n \left(|\partial_t n(t)\rangle\,\langle n(t)| - \langle n(t)|\partial_t n(t)\rangle\,|n(t)\rangle\,\langle n(t)|\right)}_{=\hat{H}_{\mathrm{CD}}} . \tag{2.16}$$

Here, $\hat{H}_{\mathrm{CD}}$ is the counterdiabatic Hamiltonian. Once we have computed $\hat{H}_{\mathrm{CD}}$, we simply need to add it to our original Hamiltonian in order to prevent diabatic evolution.

2.4.1. Landau-Zener Hamiltonian

We have already come across a variation of the Landau-Zener Hamiltonian in Eq. (2.10). The standard form reads:

$$H(t) = \frac{1}{2}\begin{bmatrix} -\Delta(t) & \Omega(t) \\ \Omega(t) & \Delta(t) \end{bmatrix}, \quad \text{where} \quad \Delta(t) \propto t \ , \tag{2.17}$$

which is identical to Eq. (2.10) up to a time-dependent energy shift that does not change the dynamics of our system. We revisit the ARP pulse example, i.e., we assume the detuning to be linear and the Rabi frequency to have a gaussian profile like in Fig. 2.2. The eigenvalues of the system are shown in Fig. 2.4; we can see an avoided crossing. The band gap determines how fast we can change the Hamiltonian without causing diabatic evolution; a large band gap permits greater speed. One can show that the counterdiabatic Hamiltonian for this system is

$$H_{\mathrm{CD}} = \begin{bmatrix} 0 & -i\dot{\theta} \\ -i\dot{\theta} & 0 \end{bmatrix}, \tag{2.18}$$

where $\theta(t) = \arctan(-\Delta(t)/\Omega(t))$, see [28, pp. 2-3]. Adding H_{CD} to the original Hamiltonian yields perfect adiabatic evolution, as we can see in Fig. 2.5. We will encounter the Landau-Zener Hamiltonian again in the subsequent chapter 3 when we study more complex systems.

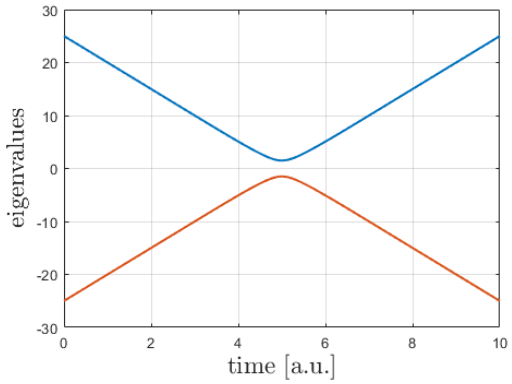

Figure 2.4.: Avoided crossing of eigenvalues of a Landau-Zener Hamiltonian where Ω has a gaussian profile and Δ is linear

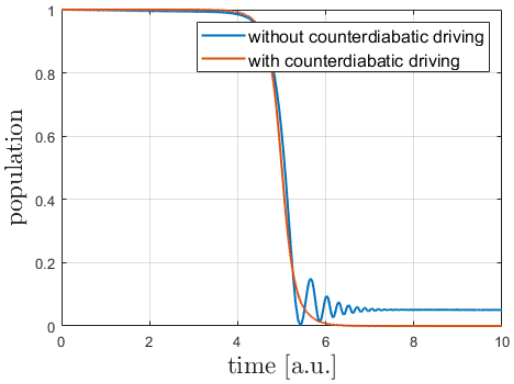

Figure 2.5.: Population transfer in a two-level system under an ARP pulse. The counterdiabatic driving clearly improves the fidelity of the transfer

2.5. Quantum gates

Classical computers are based on well-known logic gates such as the AND-, OR- and NOT gate [29, pp. 13-17]. A set of gates is said to be universal if we can construct any logic gate from this set. For instance, the AND gate and the OR gate form a universal set of classical computation [29, p. 18]. Similar to classical computation, we apply a series of quantum gates to implement quantum algorithms; each quantum gate corresponds to a unitary operation. In the following, we will give the definitions of some gates, beginning with single-qubit operations. These operations are restricted to the subspace of a single qubit. Using the basis

$\{|0\rangle, |1\rangle\}$, the matrix representation reads:

$$R_x(\theta) = \begin{bmatrix} \cos(\theta/2) & -i\sin(\theta/2) \\ -i\sin(\theta/2) & \cos(\theta/2) \end{bmatrix}, \tag{2.19}$$

$$R_y(\theta) = \begin{bmatrix} \cos(\theta/2) & -\sin(\theta/2) \\ \sin(\theta/2) & \cos(\theta/2) \end{bmatrix}, \tag{2.20}$$

$$R_z(\theta) = \begin{bmatrix} 1 & 0 \\ 0 & \exp(i\theta) \end{bmatrix}. \tag{2.21}$$

Each operation can be identified with a rotation on the Bloch sphere by the angle θ. Next, we give the matrix representation of the CNOT (=Controlled NOT) gate in the basis $\{|00\rangle, |01\rangle, |10\rangle, |11\rangle\}$.

$$\text{CNOT} = \begin{bmatrix} 1 & 0 & 0 & 0 \\ 0 & 1 & 0 & 0 \\ 0 & 0 & 0 & 1 \\ 0 & 0 & 1 & 0 \end{bmatrix} \tag{2.22}$$

As its name implies, the CNOT operation flips the target qubit if and only if the control qubit is in state $|1\rangle$. Together with single-qubit operations, the CNOT gate forms a universal set of quantum computing, i.e., any unitary operation can be expressed as a series of single-qubit gates and CNOT gates [10, p. 191]. It is well-known that the CNOT gate can be decomposed into a series of single-qubit rotations combined with a CZ gate [10, p. 294]. Using the standard basis $\{|00\rangle, |01\rangle, |10\rangle, |11\rangle\}$ again, the matrix representation of the CZ gate reads:

$$\text{CZ} = \begin{bmatrix} -1 & 0 & 0 & 0 \\ 0 & 1 & 0 & 0 \\ 0 & 0 & 1 & 0 \\ 0 & 0 & 0 & 1 \end{bmatrix}. \tag{2.23}$$

Some authors define the CZ gate such that the state $|11\rangle$ gets a π phase instead of state $|00\rangle$. An implementation of a CZ-based CNOT gate is presented in [30, p. 1]. Initially, we tried to follow this implementation, but the authors have implemented an inverted CNOT gate where the target qubit gets flipped if the control qubit is in state $|0\rangle$ instead of $|1\rangle$. To arrive at a standard CNOT gate, we added a π pulse at the beginning and the end of their protocol. The protocol in [30, p. 1] features two $\frac{\pi}{2}$ pulses that are directed at the target qubit; these pulses differ from the π pulses not only in terms of pulse area, but also in terms of relative phase, which controls the type of rotation. Unfortunately, the authors provide little information about the relative pulse phase, so we had to test different relative phases until we obtained a functioning CNOT protocol. The final protocol is depicted in Fig. 2.6.

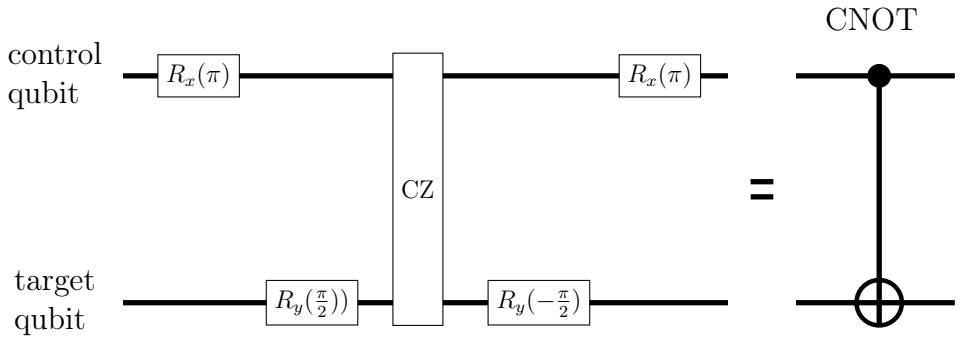

Figure 2.6.: A sequence of operations that implements a CNOT gate. The circuit symbol of a CNOT gate is shown on the right side

3. CZ gate

The entire chapter is dedicated to the CZ gate. To motivate the extensive discussion, we point out that the CZ gate is the foundation for our CNOT gate. We looked into adiabatic and nonadiabatic implementations of the CZ gate. Adiabatic gates are more robust, but this robustness comes at the expense of speed. The first section introduces a nonadiabatic CZ gate by Jaksch et al. [9, p. 2210]. After identifying an imperfection of this gate, we attempt to fix it. This is followed by a section about an adiabatic CZ implementation by Saffman et al. [31, pp. 2-4]. We chose this protocol over alternative protocols because it employs a simple one-photon excitation to populate the Rydberg state. Other protocols are based on two-photon excitations; their implementation would require a modification of our Rydberg model, since it does not feature an intermediate Rydberg level. Our contribution consists of the compensation of an unwanted phase and the application of counterdiabatic driving to the Saffman et al. protocol in order to create a fast, adiabatic CZ gate. The last section addresses the stability of our new protocol.

3.1. Nonadiabatic CZ gate

The standard approach to implement a CZ gate on the Rydberg platform was proposed by Jaksch et al. [9, p. 2210]. The paper elaborates on the implementation in the weak and strong blockade regime. We will focus on the latter. The protocol consists of three pulses: the first π normalized pulse drives the transition between $|1\rangle \leftrightarrow |r\rangle$ on the first qubit, the second 2π normalized pulse drives the transition between $|1\rangle \leftrightarrow |r\rangle$ on the second qubit, and the last pulse is identical to the first pulse. The pulse sequence is depicted in Fig. 3.1. A π pulse-induced population transfer leads to the system state gaining a dynamical phase $-\pi/2$. In theory, the computational basis $\{|00\rangle, |01\rangle, |10\rangle, |11\rangle\}$ evolves as follows:

$$|00\rangle \xrightarrow{\text{Pulse 1}} |00\rangle \xrightarrow{\text{Pulse 2}} |00\rangle \xrightarrow{\text{Pulse 3}} |00\rangle \ , \tag{3.1}$$

$$|01\rangle \xrightarrow{\text{Pulse 1}} |01\rangle \xrightarrow{\text{Pulse 2}} -|01\rangle \xrightarrow{\text{Pulse 3}} -|01\rangle \ , \tag{3.2}$$

$$|10\rangle \xrightarrow{\text{Pulse 1}} -i\,|r0\rangle \xrightarrow{\text{Pulse 2}} -i\,|r0\rangle \xrightarrow{\text{Pulse 3}} -|10\rangle \ , \tag{3.3}$$

$$|11\rangle \xrightarrow{\text{Pulse 1}} -i\,|r1\rangle \xrightarrow{\text{Pulse 2}} -i\,|r1\rangle \xrightarrow{\text{Pulse 3}} -|11\rangle \ . \tag{3.4}$$

The protocol implements the CZ gate up to an irrelevant global phase. The Rydberg blockade, which we discussed in chapter 2, sets in during the evolution of state $|11\rangle$; the first pulse excites the first qubit to $|r\rangle$. If the first qubit was not in state $|r\rangle$, the second pulse would excite the second qubit to $|r\rangle$ and back; the state

would gain a phase $-\pi$ in the process. But since the Rydberg state of the first qubit is populated, the second pulse fails to excite the second qubit to $|r\rangle$ and the system remains in state $-i\,|r1\rangle$.

3.1.1. Compensation of unwanted phase

If the Rydberg interaction V was infinite, the blockade mechanism would work perfectly, preventing the population of state $|rr\rangle$ completely. Naturally, we work with finite values for V, leading to an imperfect blockade mechanism. This results in the state $|11\rangle$ gaining a small unwanted phase $\phi_r \propto 1/\mathrm{V}$ in addition to the π phase. The other states of our computational basis are not affected since their evolution does not involve the Rydberg blockade.

It is known that the imperfect Rydberg blockade causes errors: the effect of the imperfect blockade on the CZ gate fidelity was studied in [32, pp. 11-13]. Among other imperfections, the authors discuss an error that is caused by residual population in Rydberg states; the population emerges due to the imperfect blockade. The phase error is not mentioned. Presumably, this is because the authors considered a blockade regime where the residual population error is greater than the phase error. Contrary to this, we focus on very high Rydberg interactions V such that the residual population error is negligible compared to the phase error.

A semi-analytical expression for ϕ_r can be easily obtained. It is not necessary to consider the full protocol or the full 9×9 Hamiltonian for this derivation; the blockade sets in during the second pulse, hence we focus on this part of the protocol. After we prepared our system in the initial state $|11\rangle$, the first pulse transfers the population to $|r1\rangle$; the second pulse couples this state with $|rr\rangle$, therefore we effectively consider a two-level system consisting of $|r1\rangle$ and $|rr\rangle$. The corresponding submatrix of the Hamiltonian reads

$$H(t)_{\mathrm{red}} = \begin{bmatrix} 0 & \Omega_{1r}^2/2 \\ \Omega_{1r}^2/2 & \mathrm{V} \end{bmatrix}, \tag{3.5}$$

where we used the basis $\{|r1\rangle, |rr\rangle\}$. The eigenvalues of the system are

$$E_\pm = \frac{\mathrm{V}}{2} \pm \frac{\mathrm{V}}{2}\sqrt{1 + \left(\frac{\Omega_{1r}^2}{\mathrm{V}}\right)^2}\,. \tag{3.6}$$

We argue that the states $|r1\rangle, |rr\rangle$ are approximately eigenstates of the system during the second pulse due to $|\mathrm{V}| \gg |\Omega_{1r}^2|$. The energy E_- of "eigenstate" $|r1\rangle$ can be simplified by a Taylor series at $\frac{1}{\mathrm{V}} = 0$,

$$E_- = -\frac{(\Omega_{1r}^2)^2}{4\mathrm{V}} + \mathcal{O}\left(\frac{1}{\mathrm{V}^2}\right)\,. \tag{3.7}$$

During the second pulse, state $|r1\rangle$ gains some dynamical phase which is given by the integral over the energy E_-:

$$\phi_r \approx -\int \frac{(\Omega_{1r}^2)^2}{4\mathrm{V}} dt\,, \tag{3.8}$$

where we integrate over the time interval of the second pulse. This is already our final expression for the unwanted phase since the last pulse only transfers the population of $|r1\rangle$ back to $|11\rangle$ without generating any (unwanted) phases in the process.

We found a way to compensate this phase by including a single-qubit phase gate in the original protocol and modifying the second pulse. Instead of applying a 2π normalized pulse to couple level $|1\rangle$ and $|r\rangle$ like in the original protocol, we split the second pulse into two π normalized pulses and apply a phase gate in between the pulses (see Fig. 3.1). The phase gate acts on level $|1\rangle$ of the second qubit; in matrix representation, this operation reads

$$\begin{bmatrix} 1 & 0 & 0 \\ 0 & 1 & 0 \\ 0 & 0 & 1 \end{bmatrix} \otimes \begin{bmatrix} 1 & 0 & 0 \\ 0 & e^{-i\phi_r} & 0 \\ 0 & 0 & 1 \end{bmatrix} . \tag{3.9}$$

The undesirable effect of this phase gate operation is that it affects multiple states at once; the states $|01\rangle, |11\rangle$ and $|r1\rangle$ get an additional compensation phase $-\phi_r$ (if they are populated). Our intention is to fix only the phase of initial state $|11\rangle$, but we cannot target this specific state with a single-qubit phase gate. That is why we split the second pulse into two pulses: the idea is to apply the phase gate at a time when states that should not be affected by the phase gate are not populated. We can check that our modified protocol satisfies this condition: initial state $|00\rangle$ remains unaffected by all pulses, just like in the old protocol. The initial states $|01\rangle, |10\rangle, |11\rangle$ evolve as follows:

$$|01\rangle \xrightarrow{\text{P 1}} |01\rangle \xrightarrow{\text{P 2}} -i\,|0r\rangle \xrightarrow{\text{PG}} -i\,|0r\rangle \xrightarrow{\text{P 4}} -|01\rangle \xrightarrow{\text{P 5}} -|01\rangle \ , \tag{3.10}$$

$$|10\rangle \xrightarrow{\text{P 1}} -i\,|r0\rangle \xrightarrow{\text{P 2}} -i\,|r0\rangle \xrightarrow{\text{PG}} -i\,|r0\rangle \xrightarrow{\text{P 4}} -i\,|r0\rangle \xrightarrow{\text{P 5}} -|10\rangle \ , \tag{3.11}$$

$$|11\rangle \xrightarrow{\text{P 1}} -i\,|r1\rangle \xrightarrow{\text{P 2}} -ie^{i\phi_r/2}\,|r1\rangle \xrightarrow{\text{PG}} -ie^{-i\phi_r/2}\,|r1\rangle \xrightarrow{\text{P 4}} -i\,|r1\rangle \xrightarrow{\text{P 5}} -|11\rangle \ . \tag{3.12}$$

The nth pulse is denoted by P n and the phase gate is denoted by PG. We can see that the phase gate does not interfere with the evolution of initial states $|00\rangle, |10\rangle, |01\rangle$ since these states have evolved to $|00\rangle, -i\,|r0\rangle, -i\,|0r\rangle$ at the time when we apply the phase gate. The effect of the compensation is shown in the next section.

3.1.2. Stability

To test the stability of the original protocol and study the effect of the phase compensation, we introduced a relative pulse area error ϵ on all pulses. Following an experiment conducted by Isenhower et al. [30, p. 2], we used π pulses with a length of $\sim 750\,\text{ns}$ and a Rydberg interaction $\text{V}/2\pi \approx 20\,\text{MHz}$. The fidelity was obtained via $\mathcal{F} = |\langle\phi_{\text{ini}}|\,\hat{\text{CZ}}^\dagger\,|\phi_{\text{out}}\rangle|^2$, where $\hat{\text{CZ}}$ is the operator associated with an ideal CZ operation and $|\phi_{\text{ini}}\rangle, |\phi_{\text{out}}\rangle$ are the initial / output states, respectively. Each figure shows the fidelity obtained by the original protocol as well as the fidelity

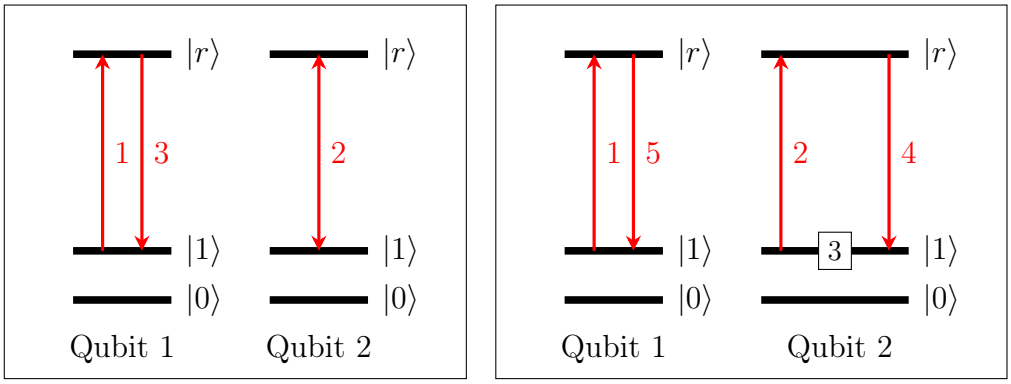

Figure 3.1.: The original CZ protocol is shown on the left side; 1 and 3 denote π pulses, 2 denotes a 2π pulse. The modified protocol is shown on the right side; 1,2,4,5 are π pulses and 3 denotes a phase gate that acts on level $|1\rangle$ of the second qubit

obtained by the modified protocol. A counterintuitive result can be observed in Fig. 3.4; a pulse area error can increase the fidelity of the original protocol in some cases, for instance if the initial state is $\frac{1}{\sqrt{2}}(|00\rangle + |11\rangle)$. Our modified protocol does not only increase the fidelity in this case, it also restores the expected behaviour by shifting the fidelity maximum back to $\epsilon = 0$, suggesting that the unexpected behaviour of the fidelity is caused by the imperfect Rydberg blockade. To confirm this hypothesis, we approximated the fidelity in the appendix A.2; our approximations are only valid in the strong blockade regime. For the initial states $|10\rangle$ and $|01\rangle$, an approximation of the fidelity is given by

$$\mathcal{F} \approx \left(1 - \frac{(\pi\epsilon)^2}{2}\right)^2 . \tag{3.13}$$

Fig. 3.2 shows that this approximation describes the fidelity very well. Our modified protocol does not improve the fidelity in this case because the evolution of $|01\rangle$ and $|10\rangle$ does not involve the Rydberg blockade, therefore there is no phase to be compensated. For the initial state $\frac{1}{\sqrt{2}}(|00\rangle + |11\rangle)$, we got the following approximation:

$$\mathcal{F} \approx \left|\frac{1}{2}\left(1 + e^{i\phi_r} + 2i\phi_r e^{i\phi_r}\epsilon + \left(\frac{\pi^2}{4} - \frac{1}{4}e^{i\phi_r}(-4i\phi_r + 8\phi_r^2 + \pi^2)\right)\epsilon^2\right)\right|^2 . \tag{3.14}$$

Here, $\phi_r = \int \frac{\Omega^2}{4V} dt$ is the unwanted phase generated by the imperfect Rydberg blockade. Fig. 3.4 shows that this approximation is only valid in a very small neighborhood of $\epsilon = 0$. Nevertheless, this expression confirms that the shift of the fidelity maximum is caused by the imperfect Rydberg blockade; if we set ϕ_r to zero, the fidelity reduces to $\mathcal{F} \equiv 1$, i.e., a small relative pulse area error does not increase the fidelity anymore. For the sake of completeness, we also give the fidelity approximation for the initial state $\frac{1}{\sqrt{2}}(|01\rangle + |11\rangle)$:

$$\mathcal{F} \approx \left|\frac{1}{2}\left(1 - \frac{(\pi\epsilon)^2}{2} + e^{i\phi_r} + 2i\phi_r e^{i\phi_r}\epsilon + \left(\frac{\pi^2}{4} - \frac{1}{4}e^{i\phi_r}(-4i\phi_r + 8\phi_r^2 + \pi^2)\right)\epsilon^2\right)\right|^2 . \tag{3.15}$$

As can be seen in Fig. 3.5, the approximation is accurate. The modified protocol performs slightly better in this case.

The fidelity improvements which we achieved by phase compensation are rather unremarkable; this can be explained by our choice of parameters. The Rydberg interaction is very strong, therefore the unwanted phase is less of an issue.

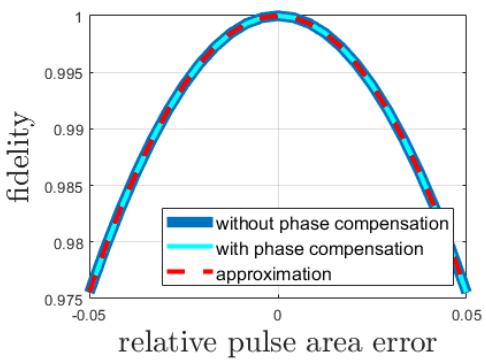

Figure 3.2.: Stability of the (un)modified CZ protocol for initial state $|01\rangle$

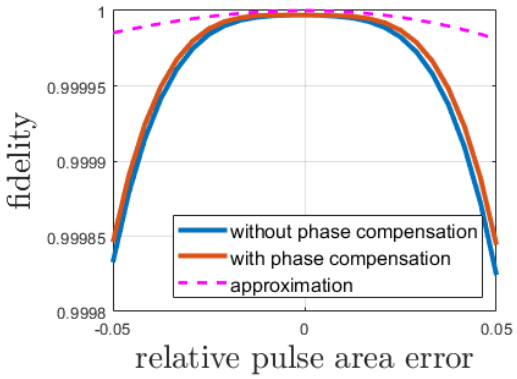

Figure 3.3.: Stability of the (un)modified CZ protocol for initial state $|11\rangle$

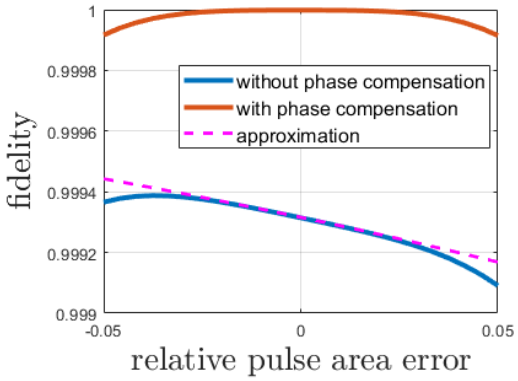

Figure 3.4.: Stability of the (un)modified CZ protocol for initial state $\frac{1}{\sqrt{2}}(|00\rangle + |11\rangle)$

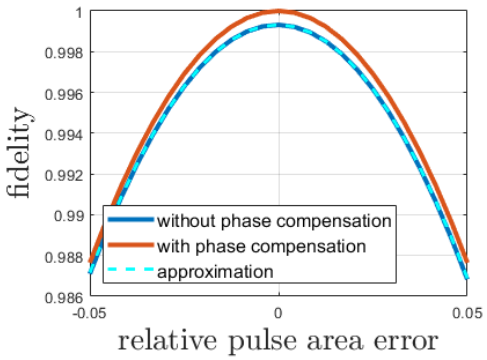

Figure 3.5.: Stability of the (un)modified CZ protocol for initial state $\frac{1}{\sqrt{2}}(|01\rangle + |11\rangle)$

3.2. Adiabatic CZ gate

An adiabatic implementation of the CZ gate was proposed in [31, pp. 2-4]. The protocol consists of two ARP pulses, which we introduced in chapter 1. The pulses act on both atoms simultaneously. The detuning and Rabi frequency are given by:

$$\Omega_{1r}^1(t) = \Omega_{1r}^2(t) = \begin{cases} \frac{\Omega_{\max}}{(1-a_1)}\left(\exp\left(-\frac{(t-T/4)^4}{\tau^4}\right) - a_1\right) & 0 \leq t \leq T/2 \\ \frac{\Omega_{\max}}{(1-a_2)}\left(\exp\left(-\frac{(t-3T/4)^4}{\tau^4}\right) - a_2\right) & T/2 \leq t \leq T \end{cases}, \tag{3.16}$$

$$\Delta^1(t) = \Delta^2(t) = \begin{cases} -\Delta_{\max}\cos\left(\frac{2\pi t}{T}\right) & 0 \leq t \leq T/2 \\ \Delta_{\max}\cos\left(\frac{2\pi t}{T}\right) & T/2 \leq t \leq T \end{cases}. \tag{3.17}$$

where $T = 0.54\,\mu s$ is the time of the protocol and $\tau = 0.175 \times T$. Since the Rabi frequency and detuning are the same for both qubits, we will omit the subscript and superscript in the following and just refer to the Rabi frequency / detuning by $\Omega(t)$ and $\Delta(t)$. The parameters a_1, a_2 are chosen such that $\Omega(0) = \Omega(T) = 0$. $\Delta_{\max}$ and $\Omega_{\max}$ are the respective maximum values. The pulse shape and the values for the parameters were taken from the paper. We used the same shapes from Eq. (3.16) and Eq. (3.17) with a minor modification concerning the smoothness of the detuning, as discussed in the next section.

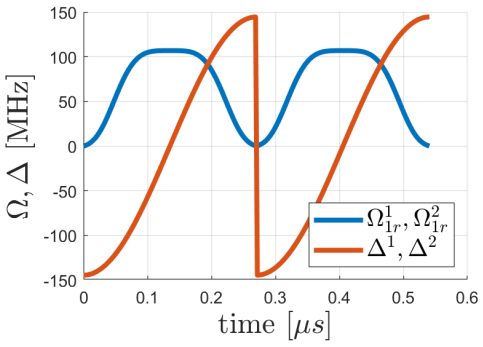

Figure 3.6.: Rabi frequency Ω and detuning Δ to implement an adiabatic CZ gate, as proposed in [31, pp. 2-4]

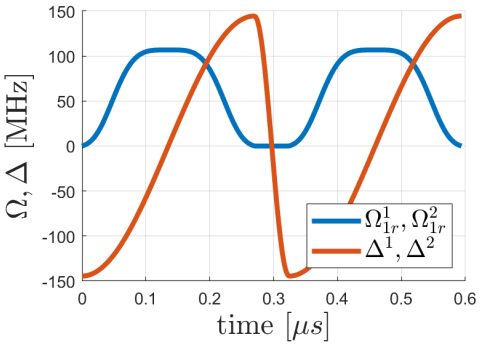

Figure 3.7.: Modified adiabatic CZ protocol with continuous detuning. The change does not impede the function of the protocol

3.2.1. Detuning jump

We denote an instantaneous eigenstate of the system by $|\phi_i\rangle$. The corresponding energy of this state is denoted by E_i. For $t \to 0$, the states satisfy:

$$|\phi_1(t)\rangle \to |00\rangle \ , \qquad |\phi_2(t)\rangle \to |01\rangle \ , \qquad |\phi_3(t)\rangle \to |0r\rangle \ , \tag{3.18}$$

$$|\phi_4(t)\rangle \to |10\rangle \ , \qquad |\phi_6(t)\rangle \to \frac{1}{\sqrt{2}}(|1r\rangle + |r1\rangle) \ , \qquad |\phi_5(t)\rangle \to |11\rangle \ , \tag{3.19}$$

$$|\phi_7(t)\rangle \to |r0\rangle \ , \qquad |\phi_8(t)\rangle \to \frac{1}{\sqrt{2}}(|1r\rangle - |r1\rangle) \ , \qquad |\phi_9(t)\rangle \to |rr\rangle \ . \tag{3.20}$$

Our computational basis is $\{|00\rangle, |01\rangle, |10\rangle, |11\rangle\}$, therefore we are particularly interested in the evolution of the eigenstates $|\phi_1(t)\rangle, |\phi_2(t)\rangle, |\phi_4(t)\rangle$ and $|\phi_5(t)\rangle$. The detuning, which is depicted in Fig. 3.6, is discontinuous. We want a more realistic temporal behaviour. To understand the purpose of the jump, we need to consider phases. During the first pulse, the states $|\phi_1(t)\rangle, |\phi_2(t)\rangle, |\phi_4(t)\rangle$ and $|\phi_5(t)\rangle$ collect some dynamical and geometric phase. The collection of geometric phase is intended, but the dynamical phase must be eliminated:

$$\int_0^T E_1(t)dt = \int_0^T E_2(t)dt = \int_0^T E_4(t)dt = \int_0^T E_5(t)dt \stackrel{!}{=} 0 \ . \tag{3.21}$$

Due to the symmetry $\Delta(t) = \Delta(t + T/2)$, the dynamical phase collected from $t = 0$ to $t = T/2$ gets cancelled by the dynamical phase collected from $t = T/2$ to $t = T$. The jump is not necessary for the compensation to work: for instance, we inserted a sine function with a duration T_2 at $t = T/2$ to create a smooth connection (see Fig. 3.7). The new protocol time is denoted by $T_{\text{tot}} = T + T_2$. There is no need to use a sine function; as long as the following conditions are satisfied, the compensation of the dynamical phase of $|\phi_1(t)\rangle, |\phi_2(t)\rangle, |\phi_4(t)\rangle$ and $|\phi_5(t)\rangle$ is guaranteed:

$$\int_{T/2}^{T/2+T_2} \Delta(t)dt = 0 \ , \qquad \Delta(T/2) = \Delta_{\max} \ , \qquad \Delta(T/2 + T_2) = -\Delta_{\max} \ . \tag{3.22}$$

We chose $T_2 = T/10$ to keep the total gate time low. The Rabi frequency remains zero during this time.

Anticipating the discussion in one of the following sections, we point out that the dynamical phase of state $|\phi_5(t)\rangle$ is not exactly equal to zero. The cause and the workaround will be discussed in section 3.2.3.

3.2.2. Counterdiabatic driving

Calculation of H_{CD} and degeneracies

To accelerate the adiabatic CZ gate while maintaining adiabatic evolution, we utilize counterdiabatic driving. In his derivation of the counterdiabatic Hamiltonian, Berry assumed the system to be nondegenerated (see section 2.4). Considering

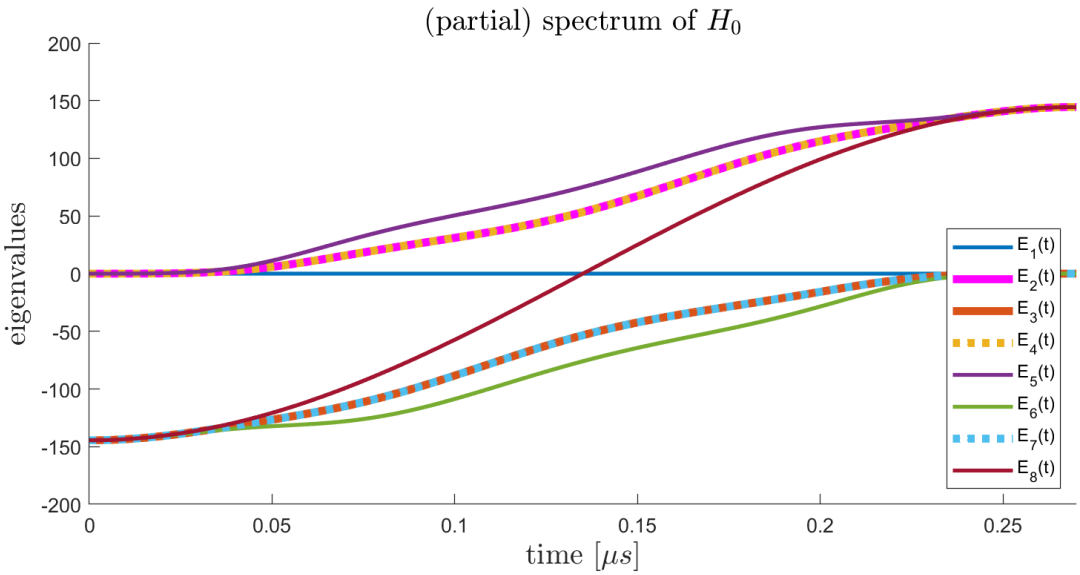

Figure 3.8.: Partial spectrum of H_0 during the first pulse; the spectrum during the second pulse is identical to this spectrum, hence we cut it off. The last eigenvalue E_9 is larger than the other eigenvalues due to the high Rydberg interaction V, therefore it is not on the scale of the figure. The avoided crossings are discussed in section 3.2.2

the spectrum of H_0 in Fig. 3.8, it seems like our system is not suited for counterdiabatic driving: it is highly degenerated. It should be noted that Fig. 3.8 only shows 8 of 9 eigenvalues; as a consequence of the high Rydberg interaction V, one eigenvalue is far greater than the others, hence it is not visible in the figure. Two of the degeneracies are maintained throughout the protocol: $E_2(t) = E_4(t)$, $E_3(t) = E_7(t)$. A general formula for counterdiabatic driving in degenerated systems does not exist, although some authors have derived formulas that allow for degeneracy under certain conditions [33, pp. 2-3]. We can argue that our system is an exception in that the degeneracies do not cause any problems. To this end, it is helpful to consider the Hamiltonian H_0:

$$H_0 = \frac{1}{2}\begin{bmatrix} 0 & 0 & 0 & 0 & 0 & 0 & 0 & 0 & 0 \\ 0 & 0 & \Omega & 0 & 0 & 0 & 0 & 0 & 0 \\ 0 & \Omega & 2\Delta & 0 & 0 & 0 & 0 & 0 & 0 \\ 0 & 0 & 0 & 0 & \Omega & 0 & 0 & 0 & 0 \\ 0 & 0 & 0 & \Omega & 2\Delta & 0 & 0 & 0 & 0 \\ 0 & 0 & 0 & 0 & 0 & 2\Delta & 0 & 0 & 0 \\ 0 & 0 & 0 & 0 & 0 & 0 & 0 & \sqrt{2}\Omega & 0 \\ 0 & 0 & 0 & 0 & 0 & 0 & \sqrt{2}\Omega & 2\Delta & \sqrt{2}\Omega \\ 0 & 0 & 0 & 0 & 0 & 0 & 0 & \sqrt{2}\Omega & 2\mathrm{V}+4\Delta \end{bmatrix} \tag{3.23}$$

First, we change to a more convenient basis to write our original Hamiltonian H_0 in block matrix form. In the basis $\{|00\rangle, |01\rangle, |0r\rangle, |10\rangle, |r0\rangle, \frac{1}{\sqrt{2}}(|1r\rangle - |r1\rangle), |11\rangle, \frac{1}{\sqrt{2}}(|1r\rangle + |r1\rangle), |rr\rangle\}$, the Hamiltonian H_0 takes the form which is shown above. The system factorizes into five subsystems that do not interact with each other; they are indicated by the red submatrices. The degeneracy is now also evident from

the Hamiltonian H_0, since the second and third submatrix-block are identical. It is readily seen that eigenvalue E_1 belongs to the first submatrix, eigenvalues E_2, E_3 belong to the second submatrix, eigenvalues E_4, E_7 belong to the third submatrix, eigenvalue E_8 belongs to the fourth submatrix and eigenvalues E_5, E_6, E_9 belong to the last submatrix. Therefore, each subsystem is nondegenerated throughout the first pulse and we can use Berry's formula for counterdiabatic driving as usual.

In a first attempt to obtain H_{CD}, we used a computer algebra program to compute the analytical eigenvalues and eigenvectors $|\phi_i(t)\rangle$ of H_0. Unfortunately, we did not succeed in obtaining an analytical expression for $\frac{\partial}{\partial t}|\phi_i(t)\rangle$, hence we only calculated a numerical approximation of H_{CD}. In order to get a numerical approximation, we diagonalized the Hamiltonian H_0 at sufficiently small equidistant time steps $\{t_j\}_{j\in J}$, which provided us with a set of eigenstates for each time step. We used a linear interpolation between the eigenstates $\{|\phi_i(t_j)\rangle\}_{j\in J}$ to get an expression for the time-dependent instantaneous eigenstates $|\phi_i(t)\rangle$. The derivative at each time step was approximated by forward differencing: $\frac{\partial}{\partial t}|\phi_i(t_j)\rangle \approx (|\phi_i(t_{j+1})\rangle - |\phi_i(t_j)\rangle)/(t_{j+1}-t_j)$; an approximation of $\frac{\partial}{\partial t}|\phi_i(t)\rangle$ is given by a further linear interpolation between $\{\frac{\partial}{\partial t}|\phi_i(t_j)\rangle\}_{j\in J}$. Even though our approach to calculating the derivative is rather primitive and the convergence of the approximation is slow, it proves to be sufficient: in general, we only need a few thousand interpolation points to obtain a counterdiabatic Hamiltonian that suppresses diabatic evolution almost perfectly. Choosing a grid with more than 5000 points is unnecessary because additional points raise the gate fidelity by at most $\sim 10^{-7}$. Since we need relatively few grid points, the derivative $\frac{\partial}{\partial t}|\phi_i(t)\rangle$ can be computed in a matter of seconds and it is not very beneficial to use a more sophisticated numerical differentiation method (five-point stencil method etc.).

Relevant entries of H_{CD}

The marked submatrices of Eq. (3.23) make it easy to understand the dynamics of the system: the evolution of the initial state $|00\rangle$ is trivial. The evolution of the initial state $|01\rangle$ is governed by the submatrix

$$\begin{bmatrix} 0 & \Omega/2 \\ \Omega/2 & \Delta \end{bmatrix}, \tag{3.24}$$

where the basis is $\{|01\rangle, |0r\rangle\}$. Given that this submatrix represents a Landau-Zener Hamiltonian, we expect one avoided crossing between the eigenstates $|\phi_2(t)\rangle$ and $|\phi_3(t)\rangle$. The symmetry of our system and our pulses dictates that the evolution of the initial state $|10\rangle$ is governed by the same submatrix, which is also evident from the Hamiltonian H_0. It follows that we can observe another avoided crossing between state $|\phi_4(t)\rangle$ and state $|\phi_7(t)\rangle$. The last 3×3 submatrix cannot be reduced, meaning that the evolution of the initial state $|11\rangle$ is complicated and the number of avoided crossings is not self-evident. The calculation of the counterdiabatic Hamiltonian shows that we have two avoided crossings: a) between state $|\phi_5(t)\rangle$ and $|\phi_6(t)\rangle$, b) between state $|\phi_5(t)\rangle$ and $|\phi_9(t)\rangle$. As previously mentioned, the

energy E_9 is a few orders of magnitude higher than the energies $E_1, ..., E_8$, thus, the avoided crossing between $|\phi_5(t)\rangle$ and $|\phi_9(t)\rangle$ has a huge band gap. We will show in the following paragraph that we do not need counterdiabatic driving to prevent this crossing. These considerations help us with construing the spectrum in Fig. 3.8. We can see the avoided crossing between E_2 and E_3 (and between E_4 / E_7), indicated by the narrowing of the lines. The avoided crossing between E_5 and E_6 is visible as well. Obviously, the avoided crossing between E_5 and E_9 is not visible, which agrees with our expectations.

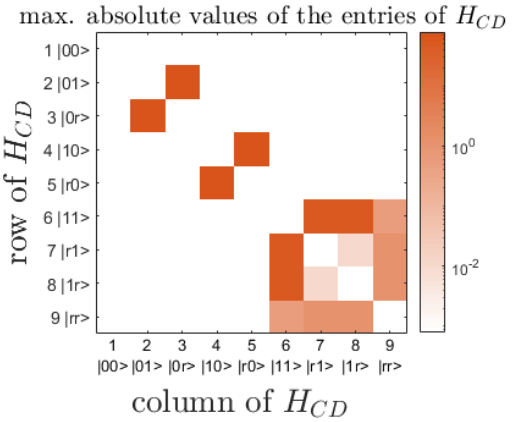

Figure 3.9.: Visualization of the entries of H_{CD}. Note that the colorbar is logarithmic

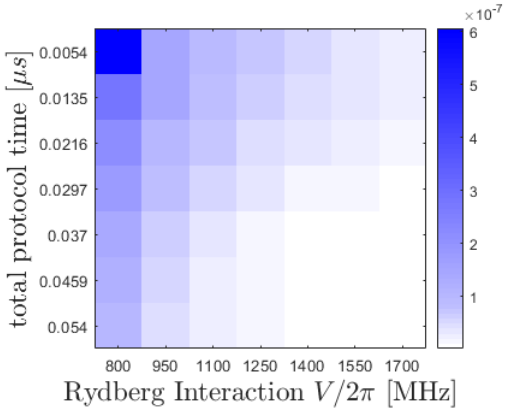

Figure 3.10.: Fidelity difference $|\mathcal{F}_1 - \mathcal{F}_2|$, where $\mathcal{F}_1$ denotes the fidelity of the protocol with full counterdiabatic driving and $\mathcal{F}_2$ denotes the fidelity of the protocol where weak entries of H_{CD} were set to zero. The initial state was $\frac{1}{\sqrt{2}}(|00\rangle + |11\rangle)$

To identify the important entries of H_{CD}, we computed $\max_{t\in[0,T_{\mathrm{tot}}]} |(H_{\mathrm{CD}}(t))_{ij}|$ for all entries $i, j = 1, ..., 9$. A qualitative comparison is shown in Fig. 3.9. From this, we conclude that the strongest couplings of the counterdiabatic Hamiltonian are $|01\rangle \leftrightarrow |0r\rangle$, $|10\rangle \leftrightarrow |r0\rangle$, $|11\rangle \leftrightarrow |1r\rangle$ and $|11\rangle \leftrightarrow |r1\rangle$. This raises the question whether the remaining couplings can be neglected to further simplify the counterdiabatic Hamiltonian. Further testing showed that we can indeed neglect these remaining entries; we computed the difference between the fidelity using the full counterdiabatic Hamiltonian and the fidelity using the simplified counterdiabatic Hamiltonian for various Rydberg interactions / protocol times. The results are shown in Fig. 3.10. Considering the structure of H_{CD}, H_0 and our previous discussion, it is clear that the weak entries of H_{CD} are meant to prevent the crossing between $|\phi_5(t)\rangle$ and $|\phi_9(t)\rangle$. Due to the huge band gap, counterdiabatic driving is not necessary for this particular crossing, which is also reflected in our results: setting weak matrix elements to zero caused a change in fidelity of order 10^{-7}, which is negligibly small. The fidelity difference changes with the Rydberg interaction V since the band gap between $|\phi_5(t)\rangle$ and $|\phi_9(t)\rangle$ depends on V. Reducing the protocol time increases the fidelity difference as well since this raises the transition

amplitudes between the eigenstates $|\phi_5(t)\rangle$ and $|\phi_9(t)\rangle$, causing the counterdiabatic driving to have a bigger effect.

It should be mentioned that all entries of the counterdiabatic Hamiltonian are imaginary. In practice, this poses a problem because it is difficult to control the relative phase of a laser and the atomic wave function in the optical regime. Without going into detail, we refer to a paper [34] that puts forward a method to simulate H_{CD} matrix elements by driven H_0 matrix elements, which solves the relative phase issue.

3.2.3. Unwanted dynamical phase

As alluded to previously in section 3.2.1, the state $|\phi_5(t)\rangle$ does not only gather a geometric phase π, but as a consequence of the imperfect Rydberg blockade, it also gathers a small dynamical phase. Note that this is not the result of a diabatic evolution, i.e., the counterdiabatic driving does not remove the phase. We encountered this problem before in section 3.1.1. The fit in Fig. 3.12 reveals that the phase is proportional to 1/V, similar to the phase in section 3.1.1. However, the derivation of a semi-analytical expression for ϕ_r proves to be more complicated than in the previous section. One way to derive this would be to calculate the analytical expression for E_5 with a computer algebra program and simplify the integral over E_5 using symmetry arguments and approximations until we get the 1/V-dependence. We want to avoid dealing with the lengthy expression for E_5, so we try a different approach: E_5 is an eigenvalue of the last submatrix in H_0, so we start with writing down the characteristic polynomial of this submatrix:

$$p(t) = -t^3 + t^2(\mathrm{V} + 3\Delta) + t(\Omega^2 - 2\Delta^2 - \Delta\mathrm{V}) - \Omega^2\Delta - \frac{1}{2}\Omega^2\mathrm{V} \,. \tag{3.25}$$

Given that $|\mathrm{V}| \gg |\Omega|, |\Delta|$, we know that one eigenvalue of the submatrix (namely the eigenvalue of $|\phi_9\rangle$) is close to V, i.e. V is approximately a root of $p(t)$, so we expand $p(t)/(t - \mathrm{V})$ in a Taylor series at $1/\mathrm{V} = 0$,

$$\frac{p(t)}{t-\mathrm{V}} = \frac{1}{2}\Omega^2 + \Delta t - t^2 + \frac{1}{\mathrm{V}}\left(\Omega^2\Delta - \frac{1}{2}\Omega^2 t + 2\Delta^2 t - 2\Delta t^2\right) + \mathcal{O}\left(\frac{1}{\mathrm{V}^2}\right) \,. \tag{3.26}$$

We neglect terms of order $\mathcal{O}\left(\frac{1}{\mathrm{V}^2}\right)$ and calculate the roots of the remaining polynomial:

$$E_\pm = \frac{1}{2(1+\frac{2\Delta}{\mathrm{V}})}\left(\Delta \pm \sqrt{-4\left(-1-\frac{2\Delta}{\mathrm{V}}\right)\left(\frac{\Omega^2}{2}+\frac{\Omega\Delta}{\mathrm{V}}\right)+\left(\Delta-\frac{\Omega^2}{2\mathrm{V}}+\frac{2\Delta^2}{\mathrm{V}}\right)^2} - \frac{\Omega^2}{2\mathrm{V}} + \frac{2\Delta^2}{\mathrm{V}}\right) \,. \tag{3.27}$$

Performing a further Taylor series at $1/\mathrm{V} = 0$ yields:

$$E_\pm = \frac{1}{2}\left(\Delta \pm \sqrt{2\Omega^2 + \Delta^2}\right) + \frac{\mp\Omega^2\Delta - \Omega^2\sqrt{2\Omega^2+\Delta^2}}{4\mathrm{V}\sqrt{2\Omega^2+\Delta^2}} + \mathcal{O}\left(\frac{1}{\mathrm{V}^2}\right) \,. \tag{3.28}$$

To check whether E_5 is approximated by E_+ or E_-, we examined the corresponding eigenvector $|\phi_5\rangle$. For times $0 \leq t \leq T_{\mathrm{tot}}/2$, the eigenvalue E_5 is approximated by

E_+. At $t = T_{\text{tot}}/2$, the submatrix is degenerated due to $\Omega(t) = \Delta(t) = 0$; we have $E_+ = E_-$, meaning that we have to reassign the eigenvalues to the eigenvectors for following times. For times $T_{\text{tot}}/2 \leq t \leq T_{\text{tot}}$, the eigenvalue E_5 is approximated by E_-,

$$E_5 \approx \begin{cases} E_+ & 0 \leq t \leq T_{\text{tot}}/2 \\ E_- & T_{\text{tot}}/2 \leq t \leq T_{\text{tot}} \end{cases} . \tag{3.29}$$

The dynamical phase of $|\phi_5\rangle$ is given by the integral over E_5. We insert our approximation and neglect terms of order $\mathcal{O}\left(\frac{1}{\text{V}^2}\right)$ once more to arrive at

$$\begin{aligned} \int_0^{T_{\text{tot}}} E_5(t)dt \approx \int_0^{T_{\text{tot}}} \Delta(t)dt + \int_0^{T_{\text{tot}}/2} \sqrt{2\Omega^2 + \Delta^2}dt - \int_{T_{\text{tot}}/2}^{T_{\text{tot}}} \sqrt{2\Omega^2 + \Delta^2}dt \\ - \int_0^{T_{\text{tot}}/2} \frac{\Omega^2\Delta}{4\text{V}\sqrt{2\Omega^2 + \Delta^2}}dt + \int_{T_{\text{tot}}/2}^{T_{\text{tot}}} \frac{\Omega^2\Delta}{4\text{V}\sqrt{2\Omega^2 + \Delta^2}}dt - \int_0^{T_{\text{tot}}} \frac{\Omega^2}{4\text{V}}dt \,. \end{aligned} \tag{3.30}$$

Now we can exploit the symmetry of the Rabi frequency and the detuning. The first, fourth and fifth integral vanish due to symmetry reasons. In addition to that, the second integral is cancelled by the third integral. By considering the remaining integral, we can see that we have derived the 1/V-dependence we were looking for:

$$\phi_r = \int_0^{T_{\text{tot}}} E_5(t)dt \approx -\int_0^{T_{\text{tot}}} \frac{\Omega^2}{4\text{V}}dt \,. \tag{3.31}$$

$$\Rightarrow \phi_r \propto \frac{T_{\text{tot}}}{\text{V}} \tag{3.32}$$

Interestingly, this expression is identical to the expression for ϕ_r in section 3.1.1 even though we considered two different protocols. There are three ways to deal with this phase: the trivial solution is to increase the Rydberg interaction V; in practice, this can be achieved by working with a higher-lying Rydberg excitation. In a sense, the counterdiabatic driving is also a solution to this problem, because it enables us to arbitrarily reduce the protocol time T_{tot}, rendering this phase insignificant. The third option is to modify the protocol in a similar fashion to our approach in section 3.1.1: we can make use of phase gates to compensate the phase. Just like in section 3.1.1, we have to insert the phase gates in such a way that they do not interfere with the evolution of initial states $|00\rangle, |01\rangle$ and $|10\rangle$. Applying a phase gate with matrix representation

$$\begin{bmatrix} 1 & 0 & 0 \\ 0 & e^{-i\phi_r} & 0 \\ 0 & 0 & 1 \end{bmatrix} \otimes \begin{bmatrix} 1 & 0 & 0 \\ 0 & e^{-i\phi_r} & 0 \\ 0 & 0 & 1 \end{bmatrix} \tag{3.33}$$

between the first and the second pulse has the intended effect, as can be readily seen: after the first pulse, the initial state $|11\rangle$ has evolved to $(|1r\rangle + |r1\rangle)/\sqrt{2}$, hence the phase gate adds a phase $-\phi_r$ to this state. The initial states $|00\rangle, |01\rangle$ and $|10\rangle$ are not affected by the phase gate, since they have evolved to $|00\rangle, |0r\rangle$

and $|r0\rangle$. We tested this compensation protocol and it seems to work well. Even so, we will refrain from using phase gates in the following because the effect of the counterdiabatic driving and the high Rydberg interaction V with which we work render the phase sufficiently small.

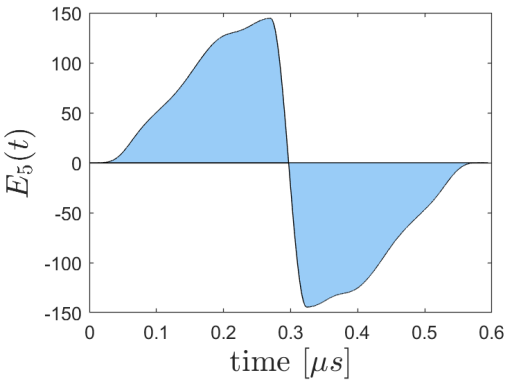

Figure 3.11.: Eigenvalue E_5 on the interval $[0, T_{\text{tot}}]$. The integral over E_5 does not vanish completely, as the figure might suggest

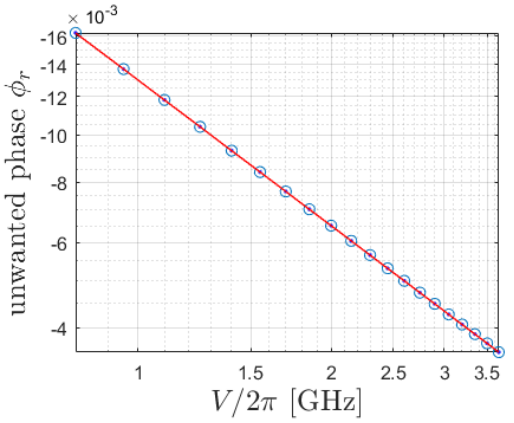

Figure 3.12.: Unwanted dynamical phase as a function of Rydberg interaction V. The red line indicates a fit $f(\text{V}) = a/\text{V}$ with one parameter a

3.2.4. Stability

The application of counterdiabatic driving to the adiabatic CZ protocol is only a viable option if the protocol remains stable. We introduced several artificial errors in our new protocol to test the stability. In the following, we used the parameters $\Omega_{\text{max}}/2\pi = 17\,\text{MHz}$, $\Delta_{\text{max}}/2\pi = 23\,\text{MHz}$, $T_{\text{tot}} = 0.0297\,\mu\text{s}$ and $\text{V}/2\pi = 1.5\,\text{GHz}$. For reasons of clarity, each plot features only three initial states: the evolution of $|00\rangle$ is trivial because the pulses do not couple to this state, so we omit this state. Besides, the evolution of $|01\rangle$ and $|10\rangle$ is analogous due to symmetry, therefore the plots only show $|01\rangle$. We also included an exemplary superposition $(|00\rangle+|11\rangle)/\sqrt{2}$ to account for phase issues that do not affect non-superpositions. The fidelity was obtained via $\mathcal{F} = |\langle\phi_{\text{ini}}|\,\hat{\text{CZ}}^\dagger\,|\phi_{\text{out}}\rangle|^2$, with $\hat{\text{CZ}}$ being the ideal CZ operator and $|\phi_{\text{ini}}\rangle, |\phi_{\text{out}}\rangle$ being the initial / output states, respectively.

Fig. 3.13 shows the effect of a relative pulse area error which was introduced on all pulses: $\Omega^\epsilon = \Omega(1+\epsilon)$. The Hamiltonian H_0 depends on the error ϵ, whereas the counterdiabatic Hamiltonian H_{CD} corresponds to the unaltered Hamiltonian H_0; if we had computed and applied the counterdiabatic Hamiltonian for each error ϵ, it would have restored the correct behaviour of the protocol and therefore we would not have seen any changes in fidelity. The effect of the error depends on the initial state; for example, the initial state $|11\rangle$ is more affected by the pulse area error than $|01\rangle$. The reason is that $|11\rangle$ evolves to $\frac{1}{\sqrt{2}}(|r1\rangle + |1r\rangle)$ and back. Some population remains in $|r1\rangle$ and $|1r\rangle$ due to the pulse area error. The initial state $|01\rangle$ evolves to $|0r\rangle$; again, some population remains in $|0r\rangle$, but the total loss of

population is smaller than for initial state $|11\rangle$, hence the fidelity is higher. The insensitivity of ARP pulses to parameter changes is also apparent from the figure: even if the pulse area has a rather large error of $\pm 5\%$, the fidelity still remains above 0.9998.

We also introduced an error on the detuning: $\Delta^\epsilon = \Delta(1+\epsilon)$. The result is shown in Fig. 3.14. The detuning error and the pulse area error seem to produce the same changes in fidelity (compare Fig. 3.14 and Fig. 3.13). There is no trivial explanation for this; one can show that the relative detuning error and the relative pulse area error result in similar transition amplitudes between the instantaneous eigenstates, which yields similar fidelities. This is discussed in more detail in the appendix A.3

Furthermore, we inserted a factor $(1+\lambda)$ to scale the counterdiabatic Hamiltonian.

$$H = H_0 + (1+\lambda)H_{\mathrm{CD}} \tag{3.34}$$

Fig. 3.15 shows the effect of this scaling factor. The system is more sensitive to this error compared to the detuning error or the pulse area error, but for $-0.025 < \lambda < 0.025$, the fidelity is still sufficiently high (> 0.995).

In addition to these errors, we also checked whether the protocol is sensitive to small delays τ_s between H_0 and H_{CD}.

$$H(t) = H_0(t) + H_{\mathrm{CD}}(t+\tau_s) \tag{3.35}$$

The result can be seen in Fig. 3.16. With regard to the stability of the protocol, this is a particularly good result: the figure shows a plateau for $-1\,\mathrm{ns} < \tau_s < +1\,\mathrm{ns}$, which amounts to roughly $\pm 3\%$ of the total protocol time. This means that small timing errors barely affect the fidelity of the protocol.

Based on these plots, we conclude that our new protocol is decently stable with regard to static pulse area / detuning errors and scaling / timing errors of H_{CD}.

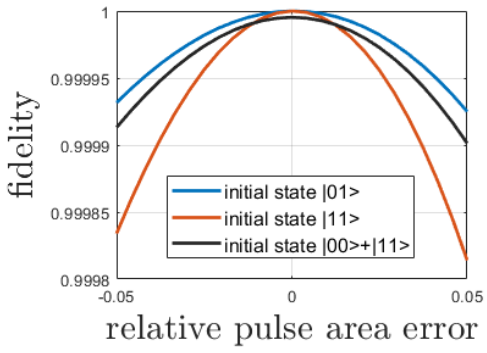

Figure 3.13.: Stability of the accelerated CZ gate with regard to relative pulse area errors

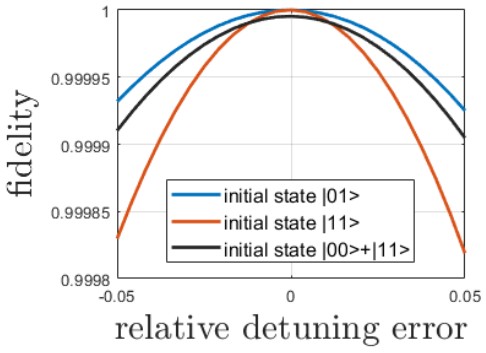

Figure 3.14.: Stability of the accelerated CZ gate with regard to relative detuning errors

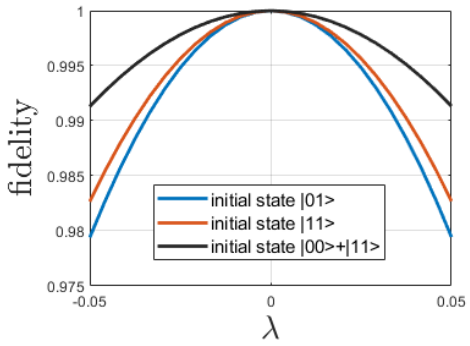

Figure 3.15.: Stability of the accelerated CZ gate with regard to scaling errors of H_{CD}

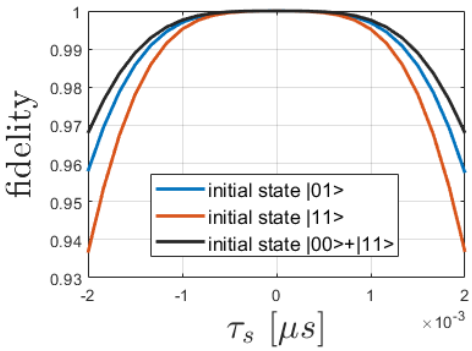

Figure 3.16.: Stability of the accelerated CZ gate with regard to time shift errors τ_s between H_0 and H_{CD}

4. CNOT gate

Having built a stable and fast CZ gate, the implementation of a CNOT gate is now straightforward. As we have shown in chapter 2, we need to add only four more pulses to the CZ protocol to obtain a CNOT gate. While this is a common approach to implement the CNOT [30, p. 1], [35, p. 3], [36, p. 3], it is not the most efficient concerning the number of pulses which are required. In particular, we also tested a (nonadiabatic) protocol [37, p. 4] that requires only four pulses in total. However, since we are especially interested in adiabatic quantum gates and the improvements that can be achieved by counterdiabatic driving, we decided to adopt the CZ approach. In this chapter, we will test the stability of our CZ-based CNOT gate. Afterwards, we will build a simple quantum error correction circuit composed of four CNOT gates, thereby demonstrating how we can unite counterdiabatic driving and quantum error correction (QEC). The QEC circuit that we will build is able to correct bit flip errors on a single qubit; more capable error correction schemes that can correct arbitrary errors on a single qubit exist, but they require more resources in terms of auxiliary qubits.

4.1. Parameters

Referring back to the decomposition of the CNOT gate (Fig. 2.6 in section 2.5), we can see that we need to perform four additional single qubit operations. The $R_x(\pi)$-rotation in the subspace of the first qubit can be implemented with a standard π pulse that we have been using throughout this thesis, but the $R_y(\frac{\pi}{2})$-rotations appear for the first time. This operation can be implemented by using a Rabi frequency with a phase shift of $\frac{\pi}{2}$; in a two-level system, the corresponding Hamiltonian reads

$$\begin{bmatrix} 0 & i\Omega(t) \\ -i\Omega(t) & \Delta(t) \end{bmatrix}, \tag{4.1}$$

where the real Rabi frequency $\Omega(t)$ is normalized to $\frac{\pi}{2}$. As we have mentioned before, in practice it is difficult to control the relative phase of a laser and the atomic wave function in the optical regime, therefore R_y-rotations are ususally decomposed into R_x- and R_z- rotations, which are easier to realize,

$$R_y(\theta) = R_x\left(\frac{\pi}{2}\right) R_z(\theta) R_x\left(-\frac{\pi}{2}\right) \ . \tag{4.2}$$

For simplicity, we will not use this decomposition since the R_y-rotations do not pose a problem in our simulation.

Up to this point, the values that we used for the Rabi frequency, Rydberg interaction etc. were based on experiments. To our knowledge, no experiment has been conducted yet that combines the adiabatic CZ gate in [31, pp. 2-4] with π pulses to create a CNOT gate, therefore we do not have any realistic values at hand for the following simulations. As a consequence, it makes sense to switch to a dimensionless framework. We introduce a characteristic time τ_0 and rewrite the Schrödinger equation as a function of $\tau = t/\tau_0$,

$$i\frac{\partial}{\partial\tau}\left|\phi(\tau)\right\rangle = \frac{\tau_0}{\hbar}\hat{H}(\tau)\left|\phi(\tau)\right\rangle \ . \tag{4.3}$$

The new time parameter τ and the new Hamiltonian $\hat{H}' = \frac{\tau_0}{\hbar}\hat{H}$ are dimensionless. Now we can choose dimensionless parameters. For simplicity, we use the same maximum value for all Rabi frequencies:

$$\max_{\tau\in[0,\tau_{\text{tot}}]}|\Omega_{01}^1(\tau)| = \max_{\tau\in[0,\tau_{\text{tot}}]}|\Omega_{01}^2(\tau)| = \max_{\tau\in[0,\tau_{\text{tot}}]}|\Omega_{1r}^1(\tau)| = \max_{\tau\in[0,\tau_{\text{tot}}]}|\Omega_{1r}^2(\tau)| = \pi \ . \tag{4.4}$$

Here, τ_{tot} denotes the total time of the CNOT protocol. In practice, the Rabi frequencies for the transitions $|0\rangle \leftrightarrow |1\rangle$ and $|1\rangle \leftrightarrow |r\rangle$ are different, but the order of magnitude should be the same. For the maximum detuning, we use $\Delta_{\text{max}} = \pi\frac{23}{17}$ such that the ratio of Δ_{max} and Ω_{max} is the same as in the previous chapter. With this choice of parameters, a discrete π pulse has the length 1 in dimensionless time units. The implementation of the adiabatic CZ gate would take ~ 20 time units if we want to make sure not to violate the adiabaticity condition, but we can accelerate this gate arbitrarily with counterdiabatic driving, so we set the CZ gate time to 2, resulting in a total CNOT protocol time of ~ 5.25 time units. Note that in theory, we do not have any lower boundary when it comes to the total gate time (except for limitations of numerical nature). We can implement π and $\frac{\pi}{2}$ pulses arbitrarily fast if we allow for large Rabi frequencies; furthermore, we can reduce the delay between pulses to zero and the counterdiabatic driving enables us to choose an arbitrary value for the CZ gate time. In practice, there are numerous limitations. The Rabi frequencies have upper limits since the laser power is limited, the pulse lengths have lower limits since we cannot switch the lasers on and off arbitrarily fast, and the counterdiabatic driving is limited as well because the entries of H_{CD} keep increasing if we reduce the protocol time. If the entries get too large, the counterdiabatic Hamiltonian cannot be realized anymore. We do not aspire to account for all of these limitations and find a realistic lower limit for the CNOT gate time, but we believe to have found a feasible degree of acceleration.

4.2. Stability

4.2.1. Propagation of phase errors

In our discussion of the CZ gate in 3.2.3, we showed that the initial state $|11\rangle$ gained a small phase ϕ_r in addition to the geometric π phase. If we do not implement any

compensation schemes, the phase error caused by the imperfect Rydberg blockade will propagate through our CNOT gate. To analyze the effect of the error quantitatively, we need to trace the evolution of the initial states of the computational basis:

$$|00\rangle \xrightarrow{\text{Pulse 1}} -i\,|10\rangle \xrightarrow{\text{Pulse 2}} -\frac{i}{\sqrt{2}}(|10\rangle + |11\rangle) \xrightarrow{\text{CZ gate}} \frac{i}{\sqrt{2}}(|10\rangle + e^{i\phi_r}\,|11\rangle)\ , \quad (4.5)$$

$$|01\rangle \xrightarrow{\text{Pulse 1}} -i\,|11\rangle \xrightarrow{\text{Pulse 2}} -\frac{i}{\sqrt{2}}(|11\rangle - |10\rangle) \xrightarrow{\text{CZ gate}} \frac{i}{\sqrt{2}}(|10\rangle - e^{i\phi_r}\,|11\rangle)\ , \quad (4.6)$$

$$|10\rangle \xrightarrow{\text{Pulse 1}} -i\,|00\rangle \xrightarrow{\text{Pulse 2}} -\frac{i}{\sqrt{2}}(|00\rangle + |01\rangle) \xrightarrow{\text{CZ gate}} \frac{i}{\sqrt{2}}(|01\rangle - |00\rangle)\ , \quad (4.7)$$

$$|11\rangle \xrightarrow{\text{Pulse 1}} -i\,|01\rangle \xrightarrow{\text{Pulse 2}} -\frac{i}{\sqrt{2}}(|01\rangle - |00\rangle) \xrightarrow{\text{CZ gate}} \frac{i}{\sqrt{2}}(|00\rangle + |01\rangle)\ . \quad (4.8)$$

It follows that the initial states $|10\rangle$ and $|11\rangle$ are not affected by the error. By considering the effect of the remaining two pulses and performing a small approximation, one can easily obtain the following result for initial states $|00\rangle$ and $|01\rangle$:

$$|00\rangle \xrightarrow{\text{CNOT}} e^{i\phi_r/2}\,|00\rangle\ , \qquad |01\rangle \xrightarrow{\text{CNOT}} e^{i\phi_r/2}\,|01\rangle\ . \quad (4.9)$$

This is a mixed result with regard to the fidelity of the CNOT operation. The unwanted phase ϕ_r is reduced by a factor of 2, but at the same time, the error has spread to another state. In the following section, we will observe that in certain cases, a series of CNOT operations can lead to an accumulation of unwanted phase, i.e., the phase can be problematic, hence it is of great importance to compensate it properly.

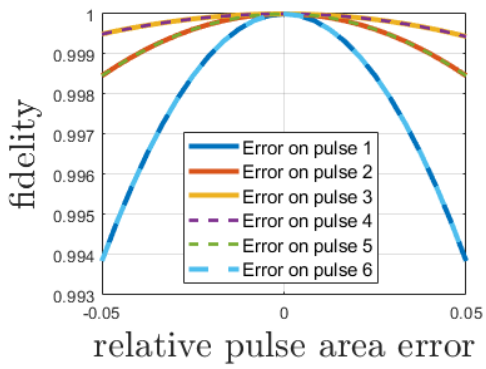

Figure 4.1.: Relative pulse area error in the CNOT protocol. The initial state was $\frac{1}{\sqrt{2}}(|00\rangle + |01\rangle)$ and the Rydberg interaction was $V = 20\Omega$

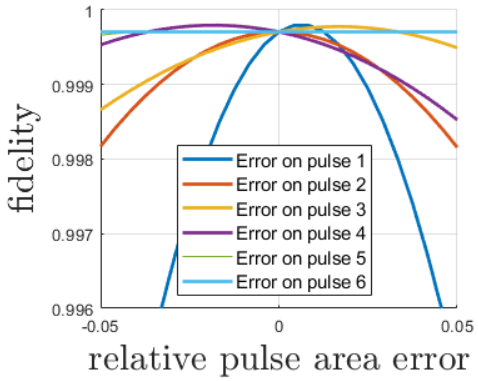

Figure 4.2.: Relative pulse area error in the CNOT protocol. The initial state was $\frac{1}{\sqrt{2}}(|00\rangle + |11\rangle)$ and the Rydberg interaction was $V = 20\Omega$

The stability analysis of the CNOT gate did not yield any particularly interesting results, that is to say, the CNOT protocol is sufficiently stable with regard to pulse area errors / detuning errors. Therefore, we restrict ourselves to showing the effect

of a relative pulse area error for two exemplary initial states. The figures show that the protocol is less sensitive to errors on the ARP pulses (pulse 3 and 4) compared to errors on the π or $\frac{\pi}{2}$ pulses; this is unsurprising since ARP pulses are more robust. Furthermore, we can see that an error can increase the fidelity, for instance if the initial state is $\frac{1}{\sqrt{2}}(|00\rangle + |11\rangle)$. We have observed this effect before when we studied the stability of the nonadiabatic CZ gate in section 3.1.2. It can be ascribed to the imperfect Rydberg blockade once again: a pulse error can partially compensate the unwanted phase, which effectively increases the fidelity. To observe this effect, we need to choose an initial state such that the CNOT operation leads to some unwanted relative phase, such as $\frac{1}{\sqrt{2}}(|00\rangle+|11\rangle) \xrightarrow{\text{CNOT}} \frac{1}{\sqrt{2}}(e^{i\phi_r/2}|00\rangle+|10\rangle)$ in Fig. 4.2. That is why we cannot observe the effect in Fig. 4.1; here, the unwanted phase is global and therefore irrelevant: $\frac{1}{\sqrt{2}}(|00\rangle+|01\rangle) \xrightarrow{\text{CNOT}} \frac{1}{\sqrt{2}}e^{i\phi_r/2}(|00\rangle+|01\rangle)$.

4.3. Quantum error correction

Quantum error correction is essential for any upcoming large-scale quantum computer to deal with errors that occur due to decoherence, faulty gate operations etc. An introduction to quantum error correction and fault-tolerant quantum computing can be found in Nielsen and Chuang [10, pp. 425-500]. In the following, we will only explain the basic idea behind the QEC circuit, as far as is needed for our application.

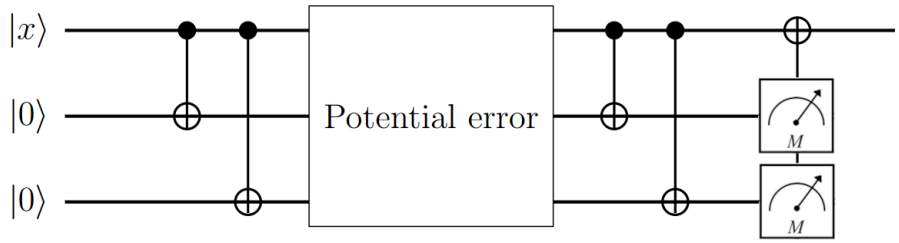

Figure 4.3.: Three-qubit quantum error correction circuit. The circuit can correct bit flips on a single qubit

The no-cloning theorem of quantum mechanics [38] states that we cannot simply make a copy of a qubit to protect the encoded information from errors. However, we can introduce auxiliary qubits to our system and encode a logical qubit in an ensemble of qubits. This is also a well-known approach in classical computing. The circuit that we will build in this section is based on three qubits; it is natural to encode the states $|0\rangle$ and $|1\rangle$ of a single logical qubit as follows:

$$|0\rangle \mapsto |000\rangle \ , \qquad |1\rangle \mapsto |111\rangle \ . \tag{4.10}$$

In general, a QEC circuit includes encoding the qubit, as well as measuring the auxiliary qubits to reveal the type of error that occured, and, if necessary, performing a recovery operation to correct the error. The set of errors that can be detected and corrected increases with the number of auxiliary qubits; for example,

Table 4.1.: Error syndrome of the three-qubit error correction circuit

Type of error	Result of measurement of qubit 2 and 3	NOT operation on qubit 1
No error	$\|00\rangle$	no
Bit flip on Qubit 1	$\|11\rangle$	yes
Bit flip on Qubit 2	$\|10\rangle$	no
Bit flip on Qubit 3	$\|01\rangle$	no

6 auxiliary qubits are sufficient to correct an arbitrary error on a single qubit (see Steane code [39]). We consider a simple error correction circuit which is depicted in Fig. 4.3. Here, qubit 1 is the qubit that we want to encode, and qubit 2 and 3 are auxiliary qubits that are prepared in state $|0\rangle$. The first two CNOT gates encode qubit 1: $\alpha|0\rangle + \beta|1\rangle \mapsto \alpha|000\rangle + \beta|111\rangle$. After the encoding phase, a potential bit flip error can occur. We will manually flip a qubit in our circuit to simulate an error. Two more CNOT operations are performed before the auxiliary qubits are measured. One can show that the measurement reveals the type of error that occured. Based on the result of the measurement, we perform a (conditional) NOT operation: the first qubit is flipped if and only if both the second and the third qubit were in state $|1\rangle$. This concludes the error correction. To compute the fidelity after the correction, we trace over the subspaces B and C of the second and third qubit, respectively,

$$\rho_{\text{reduced}} = \text{Tr}_B(\text{Tr}_C(\rho)) \ , \tag{4.11}$$

where ρ is the total density matrix of the system after we performed the QEC protocol. The fidelity can be obtained by

$$\mathcal{F} = \langle\phi_{\text{ini}}| \rho_{\text{reduced}} |\phi_{\text{ini}}\rangle \ . \tag{4.12}$$

Here, ϕ_{ini} denotes the initial state of qubit 1. So far, we only considered two-qubit systems, meaning that we have to extend our Hamiltonian in order to simulate the QEC circuit. The extensions are trivial; we add another single-qubit Hamiltonian $\hat{H}_3$ and two interaction terms to account for Rydberg interaction between the second / third and first / third qubit.

$$\begin{aligned}\hat{H} = \hat{H}_1 \otimes \mathbb{1} \otimes \mathbb{1} + \mathbb{1} \otimes \hat{H}_2 \otimes \mathbb{1} + \mathbb{1} \otimes \mathbb{1} \otimes \hat{H}_3 + \text{V}(|r\rangle\langle r| \otimes |r\rangle\langle r| \otimes \mathbb{1}) \\ + \text{V}(\mathbb{1} \otimes |r\rangle\langle r| \otimes |r\rangle\langle r|) + \text{V}(|r\rangle\langle r| \otimes \mathbb{1} \otimes |r\rangle\langle r|)\end{aligned} \tag{4.13}$$

With this extension, we can simulate the QEC circuit. The results are shown in table 4.2. The correction seems to work well, but there is some variation in fidelity depending on the initial state and the type of error. More specifically, the fidelity of the superpositions $\frac{1}{\sqrt{2}}(|0\rangle + |1\rangle)$ and $\frac{1}{\sqrt{2}}(|0\rangle + i|1\rangle)$ is slightly lower if a bit flip error occurs on the second or third qubit. This is entirely caused by the imperfect Rydberg blockade. It may seem strange that the initial states $|0\rangle$ and

Table 4.2.: Results of the error correction. While the fidelity of the correction is generally high, the imperfect Rydberg blockade can lead to accumulated phase errors that decrease the fidelity in some cases

Initial state of qubit 1	Bit flip error on qubit	Fidelity of qubit 1 after correction for V = 200Ω	Fidelity of qubit 1 after correction for V = 10Ω
$\|0\rangle$	1	>0.999999	>0.999999
	2	>0.999999	>0.999999
	3	>0.999999	>0.999999
$\|1\rangle$	1	>0.999999	>0.999999
	2	>0.999999	>0.999999
	3	>0.999999	>0.999999
$\frac{1}{\sqrt{2}}(\|0\rangle + \|1\rangle)$	1	>0.999999	>0.999999
	2	0.999985	0.993684
	3	0.999985	0.993684
$\frac{1}{\sqrt{2}}(\|0\rangle + i\,\|1\rangle)$	1	>0.999999	>0.999999
	2	0.999985	0.993684
	3	0.999985	0.993684

$|1\rangle$ are not affected; this is due to the fact that the fidelity is not an ideal measure for studying phase errors. A phase error can take the form of a global phase if we consider non-superpositions, and global phases do not decrease the fidelity. To understand why the fidelity depends on the type of error, we need to explicitly trace the evolution of each initial state once again; we skip the intermediate results here and just write down the final result for the initial state $\frac{1}{\sqrt{2}}(|0\rangle + |1\rangle)$ of qubit 1,

$$\frac{1}{\sqrt{2}}(|0\rangle + |1\rangle) \xrightarrow[\text{qubit 1 and correction}]{\text{encoding, bit flip on}} \frac{1}{\sqrt{2}}(e^{2\phi_r/2}\,|0\rangle + e^{2\phi_r/2}\,|1\rangle)\,, \tag{4.14}$$

$$\frac{1}{\sqrt{2}}(|0\rangle + |1\rangle) \xrightarrow[\text{qubit 2 and correction}]{\text{encoding, bit flip on}} \frac{1}{\sqrt{2}}(e^{4\phi_r/2}\,|0\rangle + |1\rangle)\,. \tag{4.15}$$

As we can see, the imperfect Rydberg blockade leads to an irrelevant global phase $2 \times \frac{\phi_r}{2}$ if the error occurs on qubit 2, whereas if the error occurs on qubit 2 (or 3), it leads to an accumulated relative phase $4 \times \frac{\phi_r}{2}$, which decreases the fidelity. In general, if we subject a qubit in a superposition to n subsequent CNOT operations where the qubit in question is the control qubit, it gains an unwanted relative phase of $n \times \frac{\phi_r}{2}$. In larger circuits, this phase accumulation may necessitate the implementation of a phase compensation scheme, such as the one we proposed. Obviously, for a phase compensation scheme to be effective, the leading error must be caused by the imperfect Rydberg blockade; currently, it seems like errors caused by decay processes etc. are more significant.

5. Conclusion and Outlook

5.1. Conclusion

We discussed a small unwanted phase ϕ_r that decreases the fidelity of the nonadiabatic CZ gate by Jaksch et al. [9, p. 2210]. The phase arises due to the imperfect Rydberg blockade; it is inversely proportional to the Rydberg interaction V. Only the initial state $|11\rangle$ is affected. If the Rydberg interaction V is far greater than the Rabi frequency, which is experimentally feasible, the fidelity loss due to this phase should be negligible compared to fidelity losses caused by laser imperfections, decay process etc. The Rydberg interaction V scales as n^{11} where n is the principal quantum number [40, p. 110], i.e., choosing a higher-lying Rydberg excitation is a very effective way to increase V. If, however, the range of V is limited due to experimental constraints, one can also compensate the phase ϕ_r by including a single-qubit phase gate in the protocol.

In addition to that, we accelerated an adiabatic CZ gate by Saffman et al. [31, pp. 2-4] by means of counterdiabatic driving. A stability analysis showed that the accelerated CZ gate is sufficiently stable with regard to static errors. The imperfect Rydberg blockade generates an unwanted phase again; it is identical to the phase from the nonadiabatic CZ gate. One can reduce this small phase even further by reducing the total protocol time with counterdiabatic driving or, trivially, choosing a higher Rydberg interaction V. Analogously to the nonadiabatic CZ gate, we showed that it is also possible to compensate this phase with two single-qubit phase gates.

Subsequently, we extended the accelerated CZ protocol by four pulses to obtain a CNOT protocol. The phase issue persists if we do not employ any compensation schemes to compensate ϕ_r: the initial states $|00\rangle$ and $|01\rangle$ gain an unwanted phase $\phi_r/2$ as a consequence of the CNOT operation. Finally, we built a small three-qubit error correction circuit. The circuit corrected bit flip errors on a single qubit with a high fidelity, but we observed an accumulation of phase in some cases, which illustrates the usefulness of our compensation schemes.

5.2. Outlook

The phase compensation schemes that we proposed for the nonadiabatic and adiabatic CZ gate work well in theory; however, we did not elaborate on the experimental implementation. Our schemes are based on single-qubit phase gates; this type of phase gate can, for instance, be realized by AC Stark shifts [23, p. 8]. In general,

single-qubit phase gates seem to be easy to implement [30, pp. 1-2], hence we do not anticipate any issues with the implementation of our compensation schemes.

Our simple Rydberg atom model has an obvious inaccuracy: we did not account for decay processes. Typically, the lifetime of a Rydberg state is greater than standard gate operation times, but there is some decay into hyperfine ground states as a result of spontaneous emission and stimulated emission by black-body radiation [23, p. 5]. Consequently, the gate fidelities that we computed are unrealistically high. To describe the dynamics of the system more accurately, we could move on to an open quantum system framework by substituting the Schrödinger equation for a Lindblad master equation, which allows us to account for the various decay rates. A further advantage of the master equation approach is that it allows for more sophisticated tests of the stability; we only tested the stability with regard to specific static errors, such as parameter errors. By using the master equation, we could introduce various types of noise. In a more thorough analysis, one could also account for laser crosstalk, laser phase noise, stray electric fields, Doppler-effects due to finite temperature etc. (see [41],[42]).

Furthermore, the implementation of the accelerated adiabatic CZ protocol could be the subject of future work. In its current form, the counterdiabatic Hamiltonian is of little use outside the theoretical framework. The entries of H_{CD} are imaginary, and it has been mentioned a few times before that this poses a problem since it is difficult to control the relative phase of the laser and the wave function in the optical regime. We already referred to the paper [34] that may solve this problem; the authors propose to simulate the entries of H_{CD} by modulating the original Hamiltonian H_0, which yields an effective counterdiabatic Hamiltonian. However, we have not worked out the details; the effective counterdiabatic Hamiltonian is still to be calculated and tested. We showed in section 3.2.2 that our Hamiltonian H_0 is composed of two Landau-Zener Hamiltonians, a 3×3 Hamiltonian (and two trivial 1×1 Hamiltonians); effective counterdiabatic driving for Landau-Zener systems and a similar three-level system has already been demonstrated in [34, pp. 6-10], which gives reason to believe that the method can be successfully applied to our Hamiltonian.

In this thesis, we focused on the adiabatic CZ gate proposed in [31, pp. 2-4]. It is worth mentioning that other proposals for adiabatic CZ gates have been put forward, such as [43]. It may be interesting to test whether these CZ protocols can be accelerated by counterdiabatic driving and, if so, to compare these CZ protocols to our protocol in terms of stability and feasibility.

Bibliography

[1]P. W. Shor, "Polynomial-Time Algorithms for Prime Factorization and Discrete Logarithms on a Quantum Computer", SIAM Journal on Computing **26**, 1484–1509 (1997).

[2]A. Robert, P. K. Barkoutsos, S. Woerner, and I. Tavernelli, "Resource-efficient quantum algorithm for protein folding", npj Quantum Information **7**, 38 (2021).

[3]P. Hauke, H. G. Katzgraber, W. Lechner, H. Nishimori, and W. D. Oliver, "Perspectives of quantum annealing: methods and implementations", Reports on Progress in Physics **83**, 054401 (2020).

[4]L. K. Grover, "A fast quantum mechanical algorithm for database search", in Proceedings of the Twenty-Eighth Annual ACM Symposium on Theory of Computing , STOC '96 (1996), pp. 212–219.

[5]J. Preskill, "Quantum Computing in the NISQ era and beyond", Quantum **2**, 79 (2018).

[6]J. I. Cirac and P. Zoller, "Quantum Computations with Cold Trapped Ions", Phys. Rev. Lett. **74**, 4091–4094 (1995).

[7]Y. Nakamura, Y. A. Pashkin, and J. S. Tsai, "Coherent control of macroscopic quantum states in a single-Cooper-pair box", Nature **398**, 786–788 (1999).

[8]D. Loss and D. P. DiVincenzo, "Quantum computation with quantum dots", Physical Review A **57**, 120–126 (1998).

[9]D. Jaksch, J. I. Cirac, P. Zoller, S. L. Rolston, R. Côté, and M. D. Lukin, "Fast Quantum Gates for Neutral Atoms", Physical Review Letters **85**, 2208–2211 (2000).

[10]M. A. Nielsen and I. L. Chuang, *Quantum Computation and Quantum Information, 10th anniversary edition* (Cambridge University Press, 2010).

[11]M. V. Berry, "Transitionless quantum driving", Journal of Physics A: Mathematical and Theoretical **42**, 365303 (2009).

[12]T. Albash and D. A. Lidar, "Adiabatic quantum computation", Reviews of Modern Physics **90**, 015002 (2018).

[13]D. P. DiVincenzo, "The physical implementation of quantum computation", Fortschritte der Physik **48**, 771–783 (2000).

[14]J. A. Jones, "Quantum computing and nuclear magnetic resonance", PhysChemComm **4**, 49–56 (2001).

[15]J. A. Jones, "Quantum computing with NMR", Progress in Nuclear Magnetic Resonance Spectroscopy **59**, 91–120 (2011).

[16]K. R. Brown, A. C. Wilson, Y. Colombe, C. Ospelkaus, A. M. Meier, E. Knill, D. Leibfried, and D. J. Wineland, "Single-qubit-gate error below $\mathbf{10^{-4}}$ in a trapped ion", Phys. Rev. A **84**, 030303 (2011).

[17]T. Harty, D. Allcock, C. Ballance, L. Guidoni, H. Janacek, N. Linke, D. Stacey, and D. Lucas, "High-Fidelity Preparation, Gates, Memory, and Readout of a Trapped-Ion Quantum Bit", Physical Review Letters **113**, 220501 (2014).

[18]C. J. Ballance, T. P. Harty, N. M. Linke, M. A. Sepiol, and D. M. Lucas, "High-Fidelity Quantum Logic Gates Using Trapped-Ion Hyperfine Qubits", Phys. Rev. Lett. **117**, 060504 (2016).

[19]C. Bruzewicz, J. Chiaverini, R. McConnell, and J. Sage, "Trapped-ion quantum computing: Progress and challenges", Applied Physics Reviews **6**, 021314 (2019).

[20]M. Kjaergaard, M. E. Schwartz, J. Braumüller, P. Krantz, J. I.-J. Wang, S. Gustavsson, and W. D. Oliver, "Superconducting Qubits: Current State of Play", Annual Review of Condensed Matter Physics **11**, 369–395 (2020).

[21]Y. Xu, J. Chu, J. Yuan, J. Qiu, Y. Zhou, L. Zhang, X. Tan, Y. Yu, S. Liu, J. Li, F. Yan, and D. Yu, "High-Fidelity, High-Scalability Two-Qubit Gate Scheme for Superconducting Qubits", Phys. Rev. Lett. **125**, 240503 (2020).

[22]M. Saffman, T. G. Walker, and K. Mølmer, "Quantum information with Rydberg atoms", Reviews of Modern Physics **82**, 2313–2363 (2010).

[23]M. Morgado and S. Whitlock, "Quantum simulation and computing with rydberg-interacting qubits", AVS Quantum Science **3**, 023501 (2021).

[24]M. Gärttner, "Many-Body Effects in Rydberg Gases : Coherent Dynamics of Strongly Interacting Two-Level Atoms and Nonlinear Optical Response of a Rydberg Gas in EIT Configuration", Archiv Universität Heidelberg, urn:nbn:de:bsz:16-heidok–159920 (2013).

[25]V. Malinovsky and J. Krause, "General theory of population transfer by adiabatic rapid passage with intense, chirped laser pulses", Eur. Phys. J. D **1450**, 147–155 (2001).

[26]M. Born and V. Fock, "Beweis des Adiabatensatzes. (German) [Proof of the Adiabatic Theorem]", German, **51**, 165–180 (1928).

[27]M. Demirplak and S. Rice, "Adiabatic Population Transfer with Control Fields", Journal of Physical Chemistry A - J PHYS CHEM A **107**, 46 (2003).

[28]F.-q. Dou, J. Liu, and L.-b. Fu, "High-fidelity superadiabatic population transfer of a two-level system with a linearly chirped Gaussian pulse", EPL (Europhysics Letters) **116**, 60014 (2016).

[29]D. Natarajan, "Logic gates", in *Fundamentals of digital electronics* (Springer International Publishing, Cham, 2020), pp. 13–28.

[30]L. Isenhower, E. Urban, X. L. Zhang, A. T. Gill, T. Henage, T. A. Johnson, T. G. Walker, and M. Saffman, "Demonstration of a Neutral Atom Controlled-NOT Quantum Gate", Physical Review Letters **104**, 010503 (2010).

[31]M. Saffman, I. I. Beterov, A. Dalal, E. J. Páez, and B. C. Sanders, "Symmetric Rydberg controlled-Z gates with adiabatic pulses", Phys. Rev. A **101**, 062309 (2020).

[32]M. Saffman and T. G. Walker, "Analysis of a quantum logic device based on dipole-dipole interactions of optically trapped Rydberg atoms", Physical Review A **72**, 022347 (2005).

[33]K. Takahashi, "Transitionless quantum driving for spin systems", Physical Review E **87**, 062117 (2013).

[34]F. Petiziol, B. Dive, F. Mintert, and S. Wimberger, "Fast adiabatic evolution by oscillating initial Hamiltonians", Phys. Rev. A **98**, 043436 (2018).

[35]T. Graham, M. Kwon, B. Grinkemeyer, Z. Marra, X. Jiang, M. Lichtman, Y. Sun, M. Ebert, and M. Saffman, "Rydberg-Mediated Entanglement in a Two-Dimensional Neutral Atom Qubit Array", Physical Review Letters **123**, 230501 (2019).

[36]Y. Zeng, P. Xu, X. He, Y. Liu, M. Liu, J. Wang, D. Papoular, G. Shlyapnikov, and M. Zhan, "Entangling Two Individual Atoms of Different Isotopes via Rydberg Blockade", Physical Review Letters **119**, 160502 (2017).

[37]X.-F. Shi, "Deutsch, Toffoli, and cnot Gates via Rydberg Blockade of Neutral Atoms", Phys. Rev. Applied **9**, 051001 (2018).

[38]W. K. Wootters and W. H. Zurek, "The no-cloning theorem", Physics Today **62**, 76–77 (2009).

[39]A. M. Steane, "Simple quantum error-correcting codes", Physical Review A **54**, 4741–4751 (1996).

[40]E. Urban, T. A. Johnson, T. Henage, L. Isenhower, D. D. Yavuz, T. G. Walker, and M. Saffman, "Observation of Rydberg blockade between two atoms", Nature Physics **5**, 110–114 (2009).

[41]Y. Liu, Y. Sun, Z. Fu, P. Xu, X. Wang, X. He, J. Wang, and M. Zhan, "Infidelity induced by ground-rydberg decoherence of the control qubit in a two-qubit rydberg-blockade gate", Phys. Rev. Applied **15**, 054020 (2021).

[42]S. de Lé séleuc, D. Barredo, V. Lienhard, A. Browaeys, and T. Lahaye, "Analysis of imperfections in the coherent optical excitation of single atoms to Rydberg states", Physical Review A **97**, 053803 (2018).

[43]K.-Y. Liao, X.-H. Liu, Z. Li, and Y.-X. Du, "Geometric Rydberg quantum gate with shortcuts to adiabaticity", Opt. Lett. **44**, 4801–4804 (2019).

A. Appendix

A.1. Norm preservation

We used Matlab's ode45 solver for our numerical calculations. It is based on the Dormand-Prince method, which is an embedded Runge-Kutta method. The solver compares two solutions obtained by Runge-Kutta methods of order four and five at each step; this comparison yields an estimation of the local error. If the estimated error is greater than a certain threshold ϵ, the time step size is reduced. Contrary to geometric integrators such as the Crank-Nicolson method, ode45 does not preserve the norm. Matlab allows us to manually adapt the tolerance ϵ, so we reduced the tolerance until the accuracy was acceptable. Fig. A.1 shows the norm preservation as a function of the tolerance. Here, $\mathrm{Norm}(y_{\mathrm{out}})$ is the norm of the output vector of the script. It is impractical and unnecessary to push the limits of the tolerance; the computation time increases exponentially and the changes in fidelity which we studied were of order $< 10^{-7}$, hence we usually worked with a tolerance of 10^{-9}. The figure only shows the norm preservation for the adiabatic CZ script as an example, but the norm preservation of other scripts does not differ much from this figure. In conclusion, the lack of norm preservation of our solver does not invalidate our results since we worked with a low tolerance of 10^{-9}.

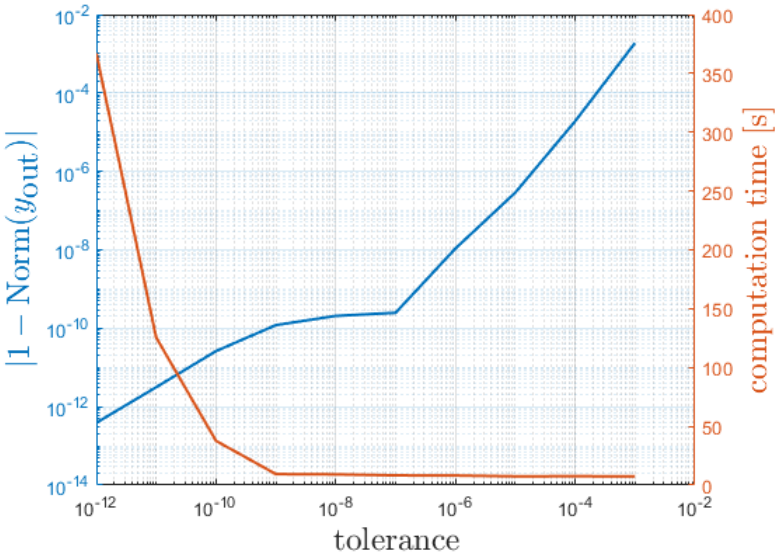

Figure A.1.: Norm preservation and computation time as a function of the tolerance of the solver

A.2. Fidelity approximation (nonadiabatic CZ gate)

We seek to derive an approximate expression for the fidelity of the nonadiabatic CZ protocol (without phase compensation) as a function of the relative pulse area error. For this purpose, we write down the unitary operators associated with the three pulses. The matrix representation of the operator corresponding to the first π pulse with a relative pulse area error ϵ reads

$$U_1(\epsilon) = \begin{bmatrix} \cos(\frac{\pi}{2}(1+\epsilon)) & -i\sin(\frac{\pi}{2}(1+\epsilon)) & 0 \\ -i\sin(\frac{\pi}{2}(1+\epsilon)) & \cos(\frac{\pi}{2}(1+\epsilon)) & 0 \\ 0 & 0 & 1 \end{bmatrix} \otimes \begin{bmatrix} 1 & 0 & 0 \\ 0 & 1 & 0 \\ 0 & 0 & 1 \end{bmatrix}, \tag{A.1}$$

where we used the single qubit basis $\{|0\rangle, |1\rangle, |r\rangle\}$. Since the third pulse is identical to the first pulse, we have $U_3(\epsilon) = U_1(\epsilon)$. Provided that $|V| \gg |\Omega|$ we can express the second pulse in the standard basis $\{|00\rangle, |01\rangle, |0r\rangle, |10\rangle, |11\rangle, |1r\rangle, |r0\rangle, |r1\rangle, |rr\rangle\}$ as

$$U_2(\epsilon) = \begin{bmatrix} 1 & 0 & 0 & 0 & 0 & 0 & 0 & 0 & 0 \\ 0 & \cos(\pi(1+\epsilon)) & -i\sin(\pi(1+\epsilon)) & 0 & 0 & 0 & 0 & 0 & 0 \\ 0 & -i\sin(\pi(1+\epsilon)) & \cos(\pi(1+\epsilon)) & 0 & 0 & 0 & 0 & 0 & 0 \\ 0 & 0 & 0 & 1 & 0 & 0 & 0 & 0 & 0 \\ 0 & 0 & 0 & 0 & \cos(\pi(1+\epsilon)) & -i\sin(\pi(1+\epsilon)) & 0 & 0 & 0 \\ 0 & 0 & 0 & 0 & -i\sin(\pi(1+\epsilon)) & \cos(\pi(1+\epsilon)) & 0 & 0 & 0 \\ 0 & 0 & 0 & 0 & 0 & 0 & 1 & 0 & 0 \\ 0 & 0 & 0 & 0 & 0 & 0 & 0 & e^{i\phi_r(1+\epsilon)^2} & 0 \\ 0 & 0 & 0 & 0 & 0 & 0 & 0 & 0 & \star \end{bmatrix} \tag{A.2}$$

where $\phi_r = \int \frac{\Omega^2}{4V} dt$ is the unwanted phase generated by the imperfect Rydberg blockade. In general, this phase depends on Ω and therefore on the relative pulse area error ϵ, but we have removed this dependence by explicitly writing $\phi_r(1+\epsilon)^2$ and assuming that ϕ_r corresponds to the unaltered Rabi frequency. The last entry of the matrix is unknown, which is indicated by the star; the state $|rr\rangle$ gains some phase, but this entry is not needed for our approximation, so we do not bother to calculate it. The 9×9 matrix $U = U_3 U_2 U_1$ represents the entire CZ protocol, but due to $|\phi_{\text{ini}}\rangle \in \text{span}(|00\rangle, |01\rangle, |10\rangle, |11\rangle)$, we only need to consider a 4×4 submatrix of U that acts on $\{|00\rangle, |01\rangle, |10\rangle, |11\rangle\}$. Let U_{red} denote this submatrix. As a reminder, the ideal CZ operation in the basis $\{|00\rangle, |01\rangle, |10\rangle, |11\rangle\}$ reads

$$\text{CZ} = \text{diag}(-1, 1, 1, 1)\ . \tag{A.3}$$

Now we can define the fidelity as follows:

$$\mathcal{F} = |\langle \phi_{\text{ini}}| \underbrace{\hat{\text{CZ}}^\dagger \hat{U}_{\text{red}}}_{=\hat{U}_{\text{tot}}} |\phi_{\text{ini}}\rangle|^2\ . \tag{A.4}$$

Here, $|\phi_{\text{ini}}\rangle$ is the initial state. A Taylor series of the 4×4 matrix representation of the operator $\hat{U}_{\text{tot}}$ at $\epsilon = 0$ yields

$$U_a = \begin{bmatrix} 1 & 0 & 0 & 0 \\ 0 & 1 - \frac{(\pi\epsilon)^2}{2} + \mathcal{O}(\epsilon^3) & -i\pi\epsilon + \mathcal{O}(\epsilon^3) & 0 \\ 0 & -i\pi\epsilon + \mathcal{O}(\epsilon^3) & 1 - \frac{(\pi\epsilon)^2}{2} + \mathcal{O}(\epsilon^3) & 0 \\ 0 & 0 & 0 & \begin{matrix} e^{i\phi_r} + 2i\phi_r e^{i\phi_r}\epsilon + \\ (\frac{\pi^2}{4} - \frac{1}{4}(-4i\phi_r + 8\phi_r^2 + \pi^2))\epsilon^2 + \mathcal{O}(\epsilon^3) \end{matrix} \end{bmatrix}, \tag{A.5}$$

where we used the basis $\{|00\rangle, |01\rangle, |10\rangle, |11\rangle\}$. This matrix allows us to give an approximation of the fidelity for arbitrary initial states and small relative pulse errors ϵ. For example, the fidelity of the CZ gate for initial state $|01\rangle$ is approximated by

$$\mathcal{F} \approx \left(1 - \frac{(\pi\epsilon)^2}{2}\right)^2. \tag{A.6}$$

A.3. Relative pulse area error and relative detuning error (adiabatic CZ gate)

We want to explain why a relative pulse area error ϵ in the adiabatic CZ protocol leads to a very similar change in fidelity as a relative detuning error ϵ (see Fig. 3.13 and 3.14). As we will see, this is due to the fact that the transition amplitudes between the instantaneous eigenstates are similar in both cases. To derive this, it is helpful to consider an alternative expression [11, p. 3] for the counterdiabatic Hamiltonian,

$$\hat{H}_{\text{CD}} = \sum_m \sum_{\substack{n \\ n \neq m}} \frac{|n\rangle \langle n| \, \partial_t \hat{H}_0 \, |m\rangle \langle m|}{E_m - E_n}. \tag{A.7}$$

Since we consider a degenerated system, it seems like we cannot apply this formula. However, we showed that our Hamiltonian factorizes into 5 nondegenerated subsystems, i.e., we can apply the formula to each subsystem. By neglecting terms that contain the large Rydberg interaction V in the denominator, we obtain

$$\begin{aligned} \hat{H}_{\text{CD}} = i\frac{\dot{\Omega}}{2\Delta}\Big[& |01\rangle \langle 01| \otimes |0r\rangle \langle 0r| + |10\rangle \langle 10| \otimes |r0\rangle \langle r0| \\ & + \frac{1}{\sqrt{2}}(|1r\rangle + |r1\rangle)(\langle 1r| + \langle r1|) \otimes |11\rangle \langle 11| + h.c.\Big]. \end{aligned} \tag{A.8}$$

Now we can easily see how the relative errors affect the counterdiabatic Hamiltonian. If we introduce a relative pulse area error $\Omega(1+\epsilon)$, the new counterdiabatic Hamiltonian is exactly given by $(1+\epsilon)\hat{H}_{\text{CD}} = \hat{H}^{\epsilon}_{\text{CD}}$. Similarly, if we introduce a relative detuning error $\Delta(1+\delta)$, the c.d. Hamiltonian is approximately given by $\frac{1}{1+\delta}\hat{H}_{\text{CD}} \approx (1-\delta)\hat{H}_{\text{CD}} = \hat{H}^{\delta}_{\text{CD}}$. When we calculated the fidelity as a function of these errors, we did not use the new c.d. Hamiltonian for each error; instead,

we used the old c.d. Hamiltonian $\hat{H}_{\text{CD}}$ that corresponded to $\hat{H}_0$ without any errors. Having derived an approximate form of the new c.d. Hamiltonian, we can rewrite the total Hamiltonian which we used to obtain the fidelity. For the case of a relative pulse area error, we write the total Hamiltonian as

$$\hat{H}_p = \hat{H}_0^\epsilon + \hat{H}_{\text{CD}} = \hat{H}_0^\epsilon + \hat{H}_{\text{CD}}^\epsilon - \epsilon \hat{H}_{\text{CD}} \ , \tag{A.9}$$

where the superscript ϵ indicates dependence on the error. The idea behind rewriting the Hamiltonian is that we now have a part $\hat{H}_0^\epsilon + \hat{H}_{\text{CD}}^\epsilon$ that yields perfect adiabatic evolution: if we change to the basis of instantaneous eigenstates, this operator will become diagonal. Let $\hat{U}_p^\epsilon$ be the corresponding change of basis operator such that $\hat{U}_p^\epsilon \hat{H}_0^\epsilon (\hat{U}_p^\epsilon)^\dagger$ is diagonal. The Hamiltonian transforms as $\hat{H}' = \hat{U}_p^\epsilon \hat{H}_{\text{old}} (\hat{U}_p^\epsilon)^\dagger + i(\partial_t \hat{U}_p^\epsilon)(\hat{U}_p^\epsilon)^\dagger$,

$$\hat{H}_p' = \underbrace{\hat{U}_p^\epsilon (\hat{H}_0^\epsilon + \hat{H}_{\text{CD}}^\epsilon)(\hat{U}_p^\epsilon)^\dagger + i(\partial_t \hat{U}_p^\epsilon)(\hat{U}_p^\epsilon)^\dagger}_{\text{diagonal operator}} - \hat{U}_p^\epsilon \epsilon \hat{H}_{\text{CD}} (\hat{U}_p^\epsilon)^\dagger \ . \tag{A.10}$$

If $\epsilon = 0$, the Hamiltonian is diagonal and the transition amplitudes between instantaneous eigenstates are zero. If $\epsilon \neq 0$, the transition amplitudes are not equal to zero since $\hat{U}_p^\epsilon \epsilon \hat{H}_{\text{CD}} (\hat{U}_p^\epsilon)^\dagger$ contains off-diagonal entries. We repeat these steps for the case of a relative detuning error.

$$\hat{H}_d = \hat{H}_0^\delta + \hat{H}_{\text{CD}} = \hat{H}_0^\delta + \hat{H}_{\text{CD}}^\delta + \delta \hat{H}_{\text{CD}} \tag{A.11}$$

Using the change of basis operator $\hat{U}_d^\delta$, we obtain

$$\hat{H}_d' = \underbrace{\hat{U}_d^\delta (\hat{H}_0^\delta + \hat{H}_{\text{CD}}^\delta)(\hat{U}_d^\delta)^\dagger + i(\partial_t \hat{U}_d^\delta)(\hat{U}_d^\delta)^\dagger}_{\text{diagonal operator}} + \hat{U}_d^\delta \delta \hat{H}_{\text{CD}} (\hat{U}_d^\delta)^\dagger \ . \tag{A.12}$$

Now we make a rough approximation: we argue that $\hat{U}_d^\delta$ and $\hat{U}_p^\epsilon$ depend only weakly on ϵ and δ compared to $\epsilon \hat{H}_{\text{CD}}$ and $\delta \hat{H}_{\text{CD}}$, so we assume $\hat{U}_d^\delta \approx \hat{U}_d^{\delta=0} = \hat{U}_p^{\epsilon=0} \approx \hat{U}_p^\epsilon$. It follows that for $\delta = \epsilon$, the last terms of $\hat{H}_p'$ and $\hat{H}_d'$ are identical up to a sign. Note that the transition amplitudes between the instantaneous eigenstates depend entirely on this last term, since the rest of the Hamiltonian is diagonal. Furthermore, the sign does not matter. We only care about the amount of population that we lose to other eigenstates as a consequence of diabatic evolution; this is not influenced by the sign. To illustrate this point, we consider initial state $|01\rangle$ in Fig. 3.13 and 3.14: ideally, this state would evolve to $-|01\rangle$ if we perform the adiabatic CZ protocol. If we introduce a relative pulse area error of 5%, the output state of the protocol is approximately $-0.99996\,|01\rangle - (0.00549 - 0.00670i)\,|0r\rangle$. Similarly, if we introduce a relative detuning error of 5%, the output state is approximately $-0.99996\,|01\rangle + (0.00548 - 0.00671i)\,|0r\rangle$. In both cases, we lost some population to $|0r\rangle$. The sign of the coefficient of $|0r\rangle$ is different, but the fidelity is the same in both cases: $\mathcal{F} = (0.99996)^2$.

Erklärung

Ich versichere, dass ich diese Arbeit selbstständig verfasst und keine anderen als die angegebenen Quellen und Hilfsmittel benutzt habe.

Freiburg, den 03.08.2022